An Efficient Inverse Finite Element Method for Shape and Stress Sensing of Laminated Composite and Sandwich Plates and Shells

Adnan Kefal
Assitant Professor
Faculty of Naval Architecture and Ocean Engineering
Istanbul Technical University, Istanbul, Turkey

Alexander Tessler
Distinguished Research Associate
Structural Mechanics and Concepts Branch
NASA Langley Research Center, Hampton, Virginia

Erkan Oterkus
Associate Professor
Department of Naval Architecture, Ocean and Marine Engineering
University of Strathclyde, Glasgow, United Kingdom

Abstract

The inverse Finite Element Method (iFEM) is a revolutionary methodology for real-time reconstruction of full-field structural displacements and stresses in structures that are instrumented with strain sensors. This inverse problem is commonly referred to as shape and stress sensing, which is well-recognized as an enabling technology for structural health monitoring systems. In this study, an improved iFEM formulation is proposed for shape and stress sensing of laminated composite and sandwich plates and shells. The formulation includes the kinematics of a shear deformation plate theory known as Refined Zigzag Theory (RZT) as its baseline. The present iFEM formulation is based upon the minimization of a weighted-least-squares functional that uses the complete set of section strains of RZT. The improved iFEM methodology is applicable for shape and stress sensing of thin and moderately thick plate and shell structures involving a relatively small number of strain gauges. The main advantage of the current formulation is that highly accurate through-the-thickness distributions of displacements, strains, and stresses are attainable using an element based on simple C^0-continuous displacement interpolation functions. A three-node inverse-shell element, named i3-RZT, is developed. Two example problems are examined in detail: (1) a simply supported rectangular laminated composite plate and (2) a wedge structure with a hole near one of the clamped ends. For both problems, the experimental strain data are generated numerically by the direct finite element analysis using high-fidelity discretizations. These strains are then regarded as the experimental strains obtained from surface mounted strain gauges or embedded fiber Bragg grating (FBG) sensors. The numerical results demonstrate the superior capability and potential applicability of the i3-RZT/iFEM methodology for performing accurate shape and stress sensing of complex composite structures.

Nomenclature

x_1, x_2, z	Cartesian coordinate system of the plate
$u_1^{(k)}, u_2^{(k)}$	In-plane displacement of the plate
u_z	Transverse displacement of the plate
u, v	Uniform through-the-thickness displacements in the x_1 and x_2 directions
w	Transverse deflection
$\phi_1^{(k)}, \phi_2^{(k)}$	Zigzag functions of RZT plate theory
ψ_1, ψ_2	Amplitude functions of the zigzag displacements
$\mathbf{u}$	Kinematic variables of RZT plate theory
$2h$	Plate thickness

$2h^{(k)}$	Thickness of the k-th lamina
$u_{(k)}, v_{(k)}$	Interfacial values of the zigzag functions
$\beta_1^{(k)}, \beta_2^{(k)}$	Slopes of the zigzag functions
$G_1,\ G_2$	Weighted-average transverse-shear moduli
$Q_{11}^{(k)},\ Q_{22}^{(k)}$	Lamina-level transverse-shear coefficients
$\varepsilon_{11}^{(k)}, \varepsilon_{22}^{(k)}, \gamma_{12}^{(k)}$	In-plane strain components
$e_\alpha\ (\alpha = 1-3),\ \mathbf{e}(\mathbf{u})$	Membrane section strains
$\kappa_\alpha\ (\alpha = 4-6),\ \boldsymbol{\kappa}(\mathbf{u})$	Bending section strains
$\mu_\alpha^{(k)}\ (\alpha = 7-9),\ \boldsymbol{\mu}^{(k)}(\mathbf{u})$	Zigzag section strains
$\mu_\alpha\ (\alpha = 7-10)$	Zigzag curvatures
$\gamma_{1z}^{(k)}, \gamma_{2z}^{(k)}$	Transverse-shear strain components
$\gamma_\alpha\ (\alpha = 10,11),\ \boldsymbol{\gamma}(\mathbf{u})$	First transverse-shear section strains
$\eta_\alpha\ (\alpha = 12,13),\ \boldsymbol{\eta}(\mathbf{u})$	Second transverse-shear section strains
$\boldsymbol{\varepsilon}_i^+, \varepsilon_{1i}^+, \varepsilon_{2i}^+, \varepsilon_{3i}^+$	Experimentally measured strains at the top surface of the laminate
$\boldsymbol{\varepsilon}_i^-, \varepsilon_{1i}^-, \varepsilon_{2i}^-, \varepsilon_{3i}^-$	Experimentally measured strains at the bottom surface of the laminate
$\boldsymbol{\varepsilon}_i^j, \varepsilon_{1i}^j, \varepsilon_{2i}^j, \varepsilon_{3i}^j$	Experimentally measured strains at the interior interface of the laminate
$\mathbf{E}_i, \mathrm{E}_{1i}, \mathrm{E}_{2i}, \mathrm{E}_{3i}$	Experimentally measured membrane strains
$\mathbf{K}_i, \mathrm{K}_{4i}, \mathrm{K}_{5i}, \mathrm{K}_{6i}$	Experimentally measured bending curvatures
$\mathbf{M}_i^j, \mathrm{M}_{7i}^j, \mathrm{M}_{8i}^j, \mathrm{M}_{9i}^j$	Experimentally measured zigzag section strains
$\mathbf{G}_i, \Gamma_{10i}, \Gamma_{11i}, \mathrm{H}_{12i}, \mathrm{H}_{13i}$	Experimentally measured transverse-shear section strains
$\mathrm{M}_\alpha\ (\alpha = 7-10)$	Experimental zigzag curvatures
$\boldsymbol{\Phi}(\mathbf{u})$	Weighted least-squares functional of total iFEM discretization
$w_\alpha\ (\alpha = 1-13)$	Positive valued weighting coefficients
$\varphi_\alpha\ (\alpha = 1-13)$	Least-squares functional of experimental section strains
x, y, z	Local coordinate system of i3-RZT element
X, Y, Z	Global coordinate system of i3-RZT element
s, t	Dimensionless parametric coordinates
$x_i, y_i\ (i = 1-3)$	Local nodal coordinates of i3-RZT element

A_e	Area of i3-RZT element
u_i , v_i , w_i	i3-RZT displacements positive along x, y, z directions
θ_{xi} , θ_{yi} , θ_{zi}	Bending and drilling rotations positive counter clockwise
ψ_{xi} , ψ_{yi} , ψ_{zi}	Zigzag and drilling rotations positive counter clockwise
N_i , L_i , M_i	Linear and quadratic interpolation functions
$\mathbf{u}^e$	Element nodal displacement vector
$\mathbf{B}_\alpha$ $(\alpha = 1-13)$	Derivatives of the shape functions
$\mathbf{\Gamma}^e$	Element left-hand-side square matrix
$\boldsymbol{\varepsilon}^e$	The element right-hand-side vector
$\mathbf{f}_\alpha^e$ $(\alpha = 1-13)$	Contribution of each experimental section strain component
$\mathbf{k}_\alpha^e$ $(\alpha = 1-13)$	Contribution of each analytic section strain component
$\mathbf{\Gamma}_\psi$	A diagonal matrix for artificial zigzag rotations
λ	Small positive constant
$k_{\psi x}^i, k_{\psi y}^i$ $(i = 1,2,3)$	Diagonal terms of $\mathbf{\Gamma}_\psi$ matrix
$\boldsymbol{\psi}_z$	Drilling zigzag DOF vector
$\mathbf{T}^e$	Transformation matrix
$\mathbf{A}$	Global left-hand-side symmetric matrix
$\mathbf{U}$	Global nodal-displacement vector
$\mathbf{Q}$	Global right-hand-side vector
nel	Total number of inverse finite elements
$\mathbf{A}_R$	Reduced form of $\mathbf{A}$ matrix
$\mathbf{Q}_R$	Reduced form of $\mathbf{Q}$ matrix
$\mathbf{U}_R$	Reduced form of $\mathbf{U}$ matrix
U, V, W	Translations along the X, Y, Z directions in Example 1
θ_X, θ_Y	Bending rotations around the positive X, Y directions in Example 1
ψ_X, ψ_Y	Zigzag rotations around the positive X, Y directions in Example 1
q	Sinusoidal varying transverse pressure in Example 1
q_0	Magnitude of sinusoidal pressure in Example 1
a , b	Length and width of the plate in Example 1

χ_{max}^{FEM} $(\chi = W, \theta_X, \theta_Y, \psi_X, \psi_Y, \sigma_v)$	Maximum values of the deflections, bending and zigzag rotations, and von Mises stresses obtained from RZT (FEM) analysis in Example 1
$\bar{\chi}$ $(\chi = W, \theta_X, \theta_Y, \psi_X, \psi_Y, \sigma_v)$	Normalized deflections, bending and zigzag rotations, and von Mises stresses obtained from i3-RZT (iFEM) analysis in Example 1
n^e	Number of element subdivisions along the plate edges in Example 1
$\bar{U}$, $\bar{\sigma}_{XX}$, $\bar{\tau}_{XZ}$	Normalized values of in-plane displacements, and normal and transverse-shear stresses in Example 1
L_1, L_2	Length and width of the wedge structure in Example 2
$(X_\alpha, Y_\alpha, Z_\alpha)$ (α=A, B)	Group coordinate systems of the wedge structure's panels A and B in Example 2
$(U_\alpha, V_\alpha, W_\alpha)$ $(\alpha = A, B)$	The translations along the positive coordinate $(X_\alpha, Y_\alpha, Z_\alpha)$ directions in Example 2
$(\theta_{X\alpha}, \theta_{Y\alpha})$ $(\alpha = A, B)$	Bending rotations around the positive (X_α, Y_α) in Example 2
$(\psi_{X\alpha}, \psi_{Y\alpha})$ $(\alpha = A, B)$	Zigzag rotations around the positive (X_α, Y_α) in Example 2
$\chi_{A,\,max}^{FEM}$, $\chi_{B,\,max}^{FEM}$ $(\chi = U, V, W, \theta_X, \theta_Y, \psi_X, \psi_Y, \sigma_v)$	Maximum values of the translations, rotations, and von Mises stress obtained from RZT (FEM) analysis for panels A and B in Example 2
$\bar{\chi}_A$, $\bar{\chi}_B$ $(\chi = U, V, W, \theta_X, \theta_Y, \psi_X, \psi_Y, \sigma_v)$	Normalized translations, rotations, and von Mises stress obtained from i3-RZT (iFEM) analysis for panels A and B in Example 2

1. Introduction

Structural health monitoring (SHM) is a multidisciplinary technology that provides conclusive real-time information regarding global and/or local structural state of a structure utilizing onboard sensing systems. The main objective of SHM is to monitor structural behavior and potentially identify damage and failure conditions. Application of SHM serves to increase human and environmental safety as well as reduce maintenance cost. Thus, SHM systems are essential technologies for many types of aeronautical, naval, and civil structures [1].

Over the last several decades, composite and sandwich material systems have been used extensively as primary structures in many different engineering applications, such as ship and offshore structures, civil and military aircraft, and wind turbines [2-4]. Such composite materials are appealing because they have superior tensile strength and resistance to compression (as a result of its fibrous nature), lighter weight, higher operating temperatures, and greater stiffness. Although composite structures offer numerous advantages, their load carrying capabilities can diminish due to various types of failures, such as delamination [5], fiber/matrix cracking [6], and face/core debonding [7], leading to severe reduction in their strength and structural integrity. Inspection of composite parts is generally cumbersome and expensive [8]. Thus, monitoring structural integrity by the way of SHM may result in improvement in safety and reduction in cost.

Real-time reconstruction of full-field structural displacements and stresses, which is commonly referred to as "shape and stress sensing", is the key component of the SHM process. A well-suited algorithm for performing shape and stress sensing of a structure should have the following characteristics: (1) general enough to take into account complex structural topologies and boundary conditions, (2) robust, stable, and accurate under a wide range of loading conditions, material systems, and inherent errors in the strain measurements, (3) sufficiently fast for real-time applications [9]. Tikhonov and Arsenin [10] introduced a regularization term that guarantees a confident smoothness degree to solve this inverse problem (shape sensing), and most of the inverse methods use some type of Tikhonov's regularization [11-13]. Many shape sensing studies have been performed to solve the problem of beam bending [14-19]. In addition to the studies concerning the shape sensing of beam-type structures, the real-time monitoring of plate structures has been considered by several authors [20-24]. Most of the inverse methods mentioned above do not take into account the complexity of boundary conditions and structural topology. They also require accurate loading information that is difficult to obtain under real-time conditions outside the laboratory environment. Hence, they are not generally suited for use in on-board SHM algorithms.

The inverse Finite Element Method (iFEM) is a state-of-the-art methodology originally introduced by Tessler and Spangler [25, 26] for real-time reconstruction of full-field structural displacements in plate and shell structures that are instrumented with strain sensors. In contrast to other developed SHM methods, the iFEM methodology is a revolutionary shape and stress sensing algorithm and possesses the aforementioned characteristics required for a powerful SHM algorithm. The main advantage of the iFEM algorithm is that static and dynamic behavior of any structure can be obtained without prior knowledge of loading. The iFEM algorithm reconstructs the structural deformations from experimentally measured strains based on the minimization of a weighted-least-squares functional. The formulation involves the entire structural geometry that is discretized by using inverse finite elements in which the measured strain data are adapted to the element strains in a least-square sense. This results in a system of linear algebraic equations that can be solved for the unknown displacements describing the deformed structural shape in real time. Recently, a U.S. patent [27] was obtained for a system that performs iFEM-based shape sensing analysis of a downhole structure for oil and gas drilling-related services.

Since the first publication of the iFEM algorithm, many different numerical and experimental studies have been devoted to expanding the horizon of the iFEM methodology in the literature. For instance, Tessler and Spangler [28] developed a three-node inverse shell element (iMIN3) utilizing lowest-order anisoparametric C^0 continuous shape functions and adopting the kinematic assumptions of Mindlin plate theory. The precision of the iMIN3 element is numerically verified in [28]. Later, Quach et al. [29] and Vazquez et al. [30] confirmed the robustness of the iMIN3 element by conducting laboratory tests that use experimentally measured real-time strain data. Moreover, Tessler et al. [31] enhanced the iMIN3 element for displacement and stress monitoring of plate and shell structures undergoing large displacements. Apart from iMIN3, Kefal et al. [32] recently formulated a four-node quadrilateral inverse-shell element, iQS4, utilizing the kinematic assumptions of the first-order and transverse-shear deformation theory. This new element includes hierarchical drilling rotation degrees-of-freedom (DOF) and further extends the practical usefulness of iFEM for shape-sensing analysis of large-scale structures. Kefal et al. [32] numerically verified the precision of the iQS4 element by solving several validation and demonstration problems. Furthermore, Cerracchio et al. [33] and Gherlone et al. [9, 34, and 35] formulated a robust inverse frame element that accounts for stretching, torsion, and 3-D bending according to Timoshenko beam theory which accounts for transverse-shear deformations. They numerically and experimentally validated the capability

of their inverse frame element by conducting several shape-sensing analyses of three-dimensional frame structures undergoing static and/or damped harmonic excitations.

The application of the iFEM methodology for SHM of future aerospace vehicles is discussed in [36, 37]. Likewise, another application of iFEM algorithm to real-time displacement monitoring of a complex geometries is presented in [38]. Apart from aerospace applications, Kefal and Oterkus [39] performed shape sensing of a longitudinally and transversely stiffened plate as a fundamental application of the iFEM framework for SHM of marine structures. Similarly, Kefal and Oterkus [40] presented a more sophisticated application of iFEM for marine structures, namely displacement and stress monitoring of a chemical tanker based on iFEM algorithm. More recently, Kefal and Oterkus [41] demonstrated the application of the iFEM methodology for monitoring multi-axial deformations and stresses of a Panamax containership advancing through sea waves. Lastly, Kefal and Oterkus [42] investigated the application of iQS4/iFEM framework to offshore structures. All investigations have so far proved that the iFEM framework is an accurate, robust, and fast shape and stress sensing algorithm.

All the iFEM-based shape sensing case studies described in the previous two paragraphs adopted First-order Shear Deformation Theory (FSDT). Although generally regarded as an accurate theory, FSDT may lead to somewhat inadequate predictions when applied to relatively thick composite and sandwich structures. For such structures, an accurate and robust formulation is required that can take into account the discrete nature of fiber- and resin-rich layers of individual plies as well as the variation of stiffness and strength properties of the core. Tessler et al. [43] developed such a formulation and called it the Refined Zigzag Theory (RZT). Recently, Cerracchio et al. [44, 45] improved the original iFEM formulation [25, 26] by adding the kinematic assumptions of the RZT. This recent formulation is intended for applications dealing with multilayered composite and sandwich structures possessing a high degree of anisotropy and heterogeneity. Even though their RZT-based iFEM formulation performs well for a wide range of composite laminates, the formulation is lacking the complete definition of transverse-shear section strains of RZT. Specifically, the variational statement invoked in Cerracchio et al. [44, 45] is simplified with respect to transverse-shear deformations: the formulation uses only the second transverse-shear section strain of RZT and omits the first transverse-shear section strain.

In the current study, the RZT-based iFEM formulation [44, 45] is enhanced to enable highly accurate shape and stress sensing of multilayered composite and sandwich plates/shells. The least-squares functional of the improved iFEM formulation is defined using the complete set of section strains consistent with RZT plate theory. These section strains are due to the membrane, bending, zigzag, and full (first and second) transverse-shear section strains. The present iFEM methodology is expected to be applicable for thin and moderately thick plate and shell structures for a wide range of laminated composites including sandwich designs. In addition, a powerful weighting strategy, originally introduced by Tessler et al. [37], is used to allow for a relatively small number of strain sensors to be utilized, thus making this new formulation to be more practical. The improved iFEM formulation requires simple C^0-continuous displacement interpolation functions. Thus, a robust and computationally efficient three-node inverse-shell element is developed (labeled as i3-RZT), which is capable of performing accurate shape- and stress-sensing analyses of complex engineering structures.

In the remainder of the paper, the theoretical foundation of the current formulation and its quantitative assessment are detailed. In section 2, the kinematics of the RZT plate theory are briefly reviewed and the strain field is properly defined in terms of all section strains to be used in the iFEM weighted-least-squares functional. In section 3, with the help of a computational procedure, experimentally measured surface

strains are used to calculate approximate transverse-shear section strains that are consistent with the experimental measurements. In section 4, a variational statement of the present iFEM methodology is introduced for both discrete and continuous forms of experimental section strains. The numerical implementation of the i3-RZT element is described based on the improved iFEM formulation in section 5. In section 6, three different simply supported rectangular laminates, each of which has a different laminate stacking sequence (uniaxial, cross-ply and angle-ply), are analyzed as a benchmark problem. Then, the applicability of the improved iFEM formulation to more complex composite/sandwich structures is demonstrated by analyzing a wedge structure with a hole near one of the clamped ends. In section 7, several conclusions emphasizing the benefits of the improved iFEM methodology are highlighted.

2. Kinematics of the Refined Zigzag Theory

A plate with thickness of $2h$ is oriented with respect to a Cartesian coordinate system (x_1, x_2, z) where (x_1, x_2) identify the mid-plane as shown in Figure 1. According to RZT plate theory [43], the orthogonal components of the displacement vector, corresponding to material points of the plate (or laminate), can be expressed as

$$u_1^{(k)}(x_1, x_2, z) \equiv u(x_1, x_2) + z\,\theta_1(x_1, x_2) + \phi_1^{(k)}(z)\,\psi_1(x_1, x_2) \tag{1a}$$

$$u_2^{(k)}(x_1, x_2, z) \equiv v(x_1, x_2) + z\,\theta_2(x_1, x_2) + \phi_2^{(k)}(z)\,\psi_2(x_1, x_2) \tag{1b}$$

$$u_z(x_1, x_2, z) \equiv w(x_1, x_2) \tag{1c}$$

where the in-plane displacement components $u_\alpha^{(k)}$ $(\alpha = 1,2)$ contain constant, linear, and zigzag variations through the thickness. The zigzag variations are C^0-continuous functions with discontinuous thickness-direction derivatives along the lamina interfaces. The superscript (k) is used to indicate the k-th lamina, whereas the subscript (k) defines the interface between the k-th and (k+1)-th laminae. Thus, the k-th lamina thickness is defined in the range $z \in [z_{(k-1)}, z_{(k)}]\,(k = 1, ..., N)$ (refer to Figure 2). The transverse displacement u_z is assumed to be constant through the thickness and is independent of constitutive properties of the k-th lamina; hence, the superscript (k) does not appear in its definition.

In Eq. (1), the functions $u = u(x_1, x_2)$ and $v = v(x_1, x_2)$ represent the mid-plane displacements (translations) along x_1 and x_2 directions, respectively. Moreover, the functions $\theta_\alpha = \theta_\alpha(x_1, x_2)$ $(\alpha = 1,2)$ represent average bending rotations of the transverse normal around the positive x_2 and negative x_1 directions, respectively. Furthermore, the function $w = w(x_1, x_2)$ is the transverse deflection and the functions $\phi_\alpha^{(k)} = \phi_\alpha^{(k)}(z)$ $(\alpha = 1,2)$ denote through-the-thickness piecewise-linear zigzag functions associated with heterogeneous plates. Finally, the functions $\psi_\alpha = \psi_\alpha(x_1, x_2)$ $(\alpha = 1,2)$ represent the spatial amplitudes of the zigzag displacements, and they are the unknowns in the analysis together with the other five kinematic variables. These functions, i.e., kinematic variables of the RZT plate theory, can be written in a compact vector form as

$$\mathbf{u} = \begin{bmatrix} u & v & w & \theta_1 & \theta_2 & \psi_1 & \psi_2 \end{bmatrix}^T \tag{2}$$

Following the approach in [43], the zigzag functions $\phi_\alpha^{(k)}$ $(\alpha = 1,2)$ can be defined as

$$\phi_1^{(k)} \equiv \frac{1}{2}(1-\xi^{(k)})u_{(k-1)} + \frac{1}{2}(1+\xi^{(k)})u_{(k)} \tag{3a}$$

$$\phi_2^{(k)} \equiv \frac{1}{2}(1-\xi^{(k)})v_{(k-1)} + \frac{1}{2}(1+\xi^{(k)})v_{(k)} \tag{3b}$$

where

$$\xi^{(k)} = \left[\frac{z-z_{(k-1)}}{h^{(k)}} - 1\right] \in [-1,1] \quad (k=1,\ldots,N) \tag{3c}$$

with the first lamina beginning at $z_{(0)} = -h$, the last (N-th) lamina ending at $z_{(N)} = +h$, and the k-th lamina ending at $z_{(k)} = z_{(k-1)} + 2h^{(k)}$, where $2h^{(k)}$ denotes the thickness of the k-th lamina.

Evaluating Eqs. (3a-b) at the lamina interfaces gives rise to the definitions of the interfacial displacements

$$\begin{aligned} &u_{(k-1)} = \phi_1^{(k)}(\xi^{(k)} = -1), \quad u_{(k)} = \phi_1^{(k)}(\xi^{(k)} = 1) \\ &v_{(k-1)} = \phi_2^{(k)}(\xi^{(k)} = -1), \quad v_{(k)} = \phi_2^{(k)}(\xi^{(k)} = 1) \quad (k = 1, \quad , N) \end{aligned} \tag{4a}$$

where the interfacial displacements at the bottom and top plate surfaces vanish identically; that is,

$$u_{(0)} = u_{(N)} = v_{(0)} = v_{(N)} = 0 \tag{4b}$$

According to Tessler et al. [43], the $u_{(k)}$ and $v_{(k)}$ interfacial values of the zigzag functions are expressed in terms of piecewise constant slope functions $\beta_\alpha^{(k)}$ $(\alpha = 1,2; k = 1, \quad , N)$ as

$$\begin{Bmatrix} u_{(k)} \\ v_{(k)} \end{Bmatrix} = 2h^{(k)} \begin{Bmatrix} \beta_1^{(k)} \\ \beta_2^{(k)} \end{Bmatrix} + \begin{Bmatrix} u_{(k-1)} \\ v_{(k-1)} \end{Bmatrix} \qquad (k = 1, \quad , N) \tag{5a}$$

where the $\beta_\alpha^{(k)}$ $(\alpha = 1,2)$ slope of the zigzag functions, namely derivatives of zigzag functions with respect to the z direction can be explicitly defined for the k-th layer as

$$\begin{Bmatrix} \beta_1^{(k)} \\ \beta_2^{(k)} \end{Bmatrix} = \begin{Bmatrix} G_1 / Q_{11}^{(k)} - 1 \\ G_2 / Q_{22}^{(k)} - 1 \end{Bmatrix} \tag{5b}$$

with

$$\begin{Bmatrix} G_1 \\ G_2 \end{Bmatrix} = \begin{Bmatrix} \left(\frac{1}{h} \sum_{i=1}^{N} \frac{h^{(i)}}{Q_{11}^{(i)}} \right)^{-1} \\ \left(\frac{1}{h} \sum_{i=1}^{N} \frac{h^{(i)}}{Q_{22}^{(i)}} \right)^{-1} \end{Bmatrix} \tag{5c}$$

where G_1 and G_2 are the weighted-average transverse shear stiffness coefficients of their respective lamina-level coefficients $Q_{11}^{(k)}$ and $Q_{22}^{(k)}$.

Using linear strain-displacement relationships of elasticity theory, the in-plane strain components can

be defined as

$$\varepsilon_{11}^{(k)} = u_{1,1}^{(k)} = e_1 + z\kappa_4 + \mu_7^{(k)} \tag{6a}$$

$$\varepsilon_{22}^{(k)} = u_{2,2}^{(k)} = e_2 + z\kappa_5 + \mu_8^{(k)} \tag{6b}$$

$$\gamma_{12}^{(k)} = u_{1,2}^{(k)} + u_{2,1}^{(k)} = e_3 + z\kappa_6 + \mu_9^{(k)} \tag{6c}$$

where $e_\alpha\ (\alpha = 1-3)$, $\kappa_\alpha\ (\alpha = 4-6)$, and $\mu_\alpha^{(k)}\ (\alpha = 7-9)$ denote the membrane, bending, and zigzag section strains (also known as strain measures.) Their explicit forms are given in terms of the kinematic variables of RZT, as

$$\mathbf{e}(\mathbf{u}) \equiv \begin{Bmatrix} e_1 \\ e_2 \\ e_3 \end{Bmatrix} = \begin{Bmatrix} u_{,1} \\ v_{,2} \\ u_{,2} + v_{,1} \end{Bmatrix} \tag{7a}$$

$$\boldsymbol{\kappa}(\mathbf{u}) \equiv \begin{Bmatrix} \kappa_4 \\ \kappa_5 \\ \kappa_6 \end{Bmatrix} = \begin{Bmatrix} \theta_{1,1} \\ \theta_{2,2} \\ \theta_{1,2} + \theta_{2,1} \end{Bmatrix} \tag{7b}$$

$$\boldsymbol{\mu}^{(k)}(\mathbf{u}) \equiv \begin{Bmatrix} \mu_7^{(k)} \\ \mu_8^{(k)} \\ \mu_9^{(k)} \end{Bmatrix} = \begin{Bmatrix} \phi_1^{(k)}\mu_7 \\ \phi_2^{(k)}\mu_8 \\ \phi_1^{(k)}\mu_9 + \phi_2^{(k)}\mu_{10} \end{Bmatrix} \tag{7c}$$

with

$$\begin{bmatrix} \mu_7 & \mu_8 & \mu_9 & \mu_{10} \end{bmatrix} = \begin{bmatrix} \psi_{1,1} & \psi_{2,2} & \psi_{1,2} & \psi_{2,1} \end{bmatrix} \tag{7d}$$

where $\mu_\alpha\ (\alpha = 7-10)$ represents the zigzag curvatures. Note that the zigzag section strains $\boldsymbol{\mu}^{(k)}(\mathbf{u})$, the zigzag functions $\phi_\alpha^{(k)}\ (\alpha = 1,2)$, and the zigzag curvatures $\mu_\alpha\ (\alpha = 7-10)$ are coupled in Eq. (7c).

The transverse-shear strain components can be defined as

$$\gamma_{1z}^{(k)} = u_{1,z}^{(k)} + u_{z,1} = (1 + \beta_1^{(k)})\,\gamma_{10} - \beta_1^{(k)}\eta_{12} \tag{8a}$$

$$\gamma_{2z}^{(k)} = u_{2,z}^{(k)} + u_{z,2} = (1 + \beta_2^{(k)})\,\gamma_{11} - \beta_2^{(k)}\eta_{13} \tag{8b}$$

where $\gamma_\alpha\ (\alpha = 10,11)$ and $\eta_\alpha\ (\alpha = 12,13)$ denote, respectively, the first and second transverse-shear section strains of RZT. Their explicit forms in terms of the kinematic variables $\mathbf{u}$ are given as

$$\boldsymbol{\gamma}(\mathbf{u}) \equiv \begin{Bmatrix} \gamma_{10} \\ \gamma_{11} \end{Bmatrix} = \begin{Bmatrix} w_{,1} + \theta_1 \\ w_{,2} + \theta_2 \end{Bmatrix} \tag{9a}$$

$$\boldsymbol{\eta}(\mathbf{u}) \equiv \begin{Bmatrix} \eta_{12} \\ \eta_{13} \end{Bmatrix} = \begin{Bmatrix} \gamma_{10} - \psi_1 \\ \gamma_{11} - \psi_2 \end{Bmatrix} \tag{9b}$$

Integrating Eq. (8) across the laminate thickness while normalizing by the laminate thickness gives the

average transverse-shear section strains

$$\begin{Bmatrix}\gamma_{10}\\ \gamma_{11}\end{Bmatrix}=\frac{1}{2h}\int_{-h}^{h}\begin{Bmatrix}\gamma_{1z}^{(k)}\\ \gamma_{2z}^{(k)}\end{Bmatrix}dz \tag{10}$$

Note that γ_α $(\alpha=10,11)$ have the same definition as the transverse-shear strains of FSDT; moreover, the zigzag rotations ψ_α $(\alpha=1,2)$ provide no contribution to these average transverse-shear strains.

3. Computation of experimental section strains

Conventional strain rosettes or embedded fiber-optic strain sensor networks (e.g., Fiber Bragg Grating (FBG) sensors) can be used to provide a large amount of on-board strain data that is required by the iFEM computational framework. Since RZT requires three strain sensors in the thickness direction for a given in-plane position (refer to Figure 3), the most natural sensor positions are top and bottom surface-mounted sensors and, in addition, an embedded sensor between any two adjacent material layers. The subject of how to embed FBG strain sensors in laminated composites, addressing issues of durability and survivability, has been recently discussed in [55]. The optical fiber can be directly positioned between the plies at the desired locations during the hand lay-up manufacturing process. In addition, the automated manufacturing process with fiber placement robot technology can be used to embed the optical fibers. Alternatively, embedding-after-manufacturing can also be implemented by creating hollow tubes during the curing process of the laminate. Subsequently, the optical fiber can be positioned through the hollow tube and fixed in position by injection of epoxy resin.

The first step in this formulation requires the knowledge of all section strains of RZT, those computed from the theory itself (analytic section strains, Eqs. (7) and (9)), and those computed from the actual strain measurements (experimental strains). The following notation is used to denote experimentally measured strains that are measured at the top '+', bottom '–', and interior interface 'j' locations

$$\boldsymbol{\varepsilon}_i^{+}(\mathbf{x}_i,z_i=+h)=[\varepsilon_{1i}^{+}\quad\varepsilon_{2i}^{+}\quad\varepsilon_{3i}^{+}] \tag{11a}$$

$$\boldsymbol{\varepsilon}_i^{-}(\mathbf{x}_i,z_i=-h)=[\varepsilon_{1i}^{-}\quad\varepsilon_{2i}^{-}\quad\varepsilon_{3i}^{-}] \tag{11b}$$

$$\boldsymbol{\varepsilon}_i^{j}(\mathbf{x}_i,z_i=z_{(j)})=[\varepsilon_{1i}^{j}\quad\varepsilon_{2i}^{j}\quad\varepsilon_{3i}^{j}] \tag{11c}$$

where in $(\varepsilon_{\alpha i}^{+},\varepsilon_{\alpha i}^{-},\varepsilon_{\alpha i}^{j})$ $(\alpha=1,2,3)$ the first subscripts 1 and 2 denote the transformed normal strain measurement along the directions x_1 and x_2, whereas the first subscript 3 denotes the transformed shear strains in the x_1x_2 plane.

By virtue of the zigzag functions of RZT, the zigzag contributions to the in-plane strains vanish at the top and bottom surfaces. Therefore, the experimentally measured membrane strains $\mathbf{E}_i$ and bending curvatures $\mathbf{K}_i$ can be determined at a particular discrete location $\mathbf{x}_i$ as

$$\mathbf{E}_i\equiv\begin{Bmatrix}\mathrm{E}_1\\ \mathrm{E}_2\\ \mathrm{E}_3\end{Bmatrix}_i=\frac{1}{2}\begin{Bmatrix}\varepsilon_1^{+}+\varepsilon_1^{-}\\ \varepsilon_2^{+}+\varepsilon_2^{-}\\ \varepsilon_3^{+}+\varepsilon_3^{-}\end{Bmatrix}_i \tag{12a}$$

$$\mathbf{K}_i \equiv \begin{Bmatrix} \mathrm{K}_4 \\ \mathrm{K}_5 \\ \mathrm{K}_6 \end{Bmatrix}_i = \frac{1}{2h} \begin{Bmatrix} \varepsilon_1^+ - \varepsilon_1^- \\ \varepsilon_2^+ - \varepsilon_2^- \\ \varepsilon_3^+ - \varepsilon_3^- \end{Bmatrix}_i \tag{12b}$$

The $\mathbf{E}_i$ and $\mathbf{K}_i$ section strains correspond to their analytic counterparts $\mathbf{e}(\mathbf{u})$ and $\boldsymbol{\kappa}(\mathbf{u})$ given by Eqs. (7a-b).

Substituting *j*-th interface measured strains $\varepsilon_{\alpha i}^j$ $(\alpha = 1,2,3)$ and section strains $\mathbf{E}_i$ and $\mathbf{K}_i$ into Eq. (6), the $\mathbf{M}_i^j$ zigzag section strains can be computed at a particular discrete location $(\mathbf{x}_i, z_i = z_{(j)})$ as [44, 45]

$$\mathbf{M}_i^j \equiv \begin{Bmatrix} \mathrm{M}_7^j \\ \mathrm{M}_8^j \\ \mathrm{M}_9^j \end{Bmatrix}_i = \begin{Bmatrix} \varepsilon_1^j - \mathrm{E}_1 - z_{(j)} \mathrm{K}_4 \\ \varepsilon_2^j - \mathrm{E}_2 - z_{(j)} \mathrm{K}_5 \\ \varepsilon_3^j - \mathrm{E}_3 - z_{(j)} \mathrm{K}_6 \end{Bmatrix}_i \tag{13}$$

Note that the internal strain sensors can be positioned along any layer interface $z_{(j)}$ and that $\mathbf{M}_i^j$ are evaluated at that interface. Hence, when $\mathbf{M}_i^j$ is compared to its analytic counterpart $\boldsymbol{\mu}^{(k)}(\mathbf{u})$ within the iFEM/RZT variational equation (refer to Section 4), both terms are evaluated at the same location $(\mathbf{x}_i, z_i = z_{(j)})$. The uppercase Greek letters in Eqs. (12-13) are used herein to denote the section strains due to experimental measurements.

The transverse-shear section strains can be cast in vector form as

$$\mathbf{G}_i = \begin{bmatrix} \Gamma_{10} & \Gamma_{11} & \mathrm{H}_{12} & \mathrm{H}_{13} \end{bmatrix}_i \tag{14}$$

where $\Gamma_{\alpha i}$ $(\alpha = 10,11)$ and $\mathrm{H}_{\alpha i}$ $(\alpha = 12,13)$ denote discrete first and second transverse-shear section strains that correspond to their analytic counterparts $\boldsymbol{\gamma}(\mathbf{u})$ and $\boldsymbol{\eta}(\mathbf{u})$ given respectively by Eq. (9a-b).

The experimentally measured strains $(\varepsilon_{\alpha i}^+, \varepsilon_{\alpha i}^-, \varepsilon_{\alpha i}^j)$ $(\alpha = 1,2,3)$ cannot be directly used to calculate the transverse-shear section strains $\mathbf{G}_i$. It is noted that in thin shells, the contributions of $\mathbf{G}_i$ are very small in comparison to those due to bending and zigzag curvatures. In this case, the $\mathbf{G}_i$ contributions can be safely omitted from the iFEM formulation. On the other hand, in thick shells, a significant amount of deformation is caused by transverse-shear stresses; consequently, shear deformation, hence $\mathbf{G}_i$ must be included in the iFEM analysis.

The discrete $\mathbf{E}_i$, $\mathbf{K}_i$, and $\mathbf{M}_i^j$ quantities can also be smoothed a priori utilizing, for example, the Smoothing Element Analysis (SEA) developed by Tessler et al. [46, 47]. Upon SEA smoothing, these quantities are represented by nearly C^1-continuous, piecewise polynomials with C^0-continuous first-order derivatives. The smoothed counterparts of these experimental section strains will henceforth be denoted as $\mathbf{E}$, $\mathbf{K}$, and $\mathbf{M}^j$, where the '*i*' subscript is removed to differentiate them from the discrete quantities. An additional advantage of this smoothing step is that sufficiently accurate first-order derivatives of $\mathbf{E}$, $\mathbf{K}$, and $\mathbf{M}^j$ can be obtained and subsequently used to obtain sufficiently accurate estimates of the corresponding transverse-shear section strains $\mathbf{G}$. The requisite steps in the computational procedure to calculate $\mathbf{G}$ are described in Figure 4. In this procedure, four equilibrium equations of RZT are solved for

the transverse-shear stress resultants [43], while requiring $\mathrm{M}_\alpha\ (\alpha=7-10)$ (experimental zigzag curvatures) to be continuous. These curvatures correspond to their analytic counterparts $\mu_\alpha\ (\alpha=7-10)$ given by Eq. (7d). The continuous form of $\mathrm{M}_\alpha\ (\alpha=7,8)$ can be readily obtained from $\mathrm{M}_\alpha^j\ (\alpha=7,8)$ as

$$\begin{Bmatrix}\mathrm{M}_7\\ \mathrm{M}_8\end{Bmatrix}=\begin{Bmatrix}\dfrac{\mathrm{M}_7^j}{\phi_1^{(k)}(z_{(j)})}\\ \dfrac{\mathrm{M}_8^j}{\phi_2^{(k)}(z_{(j)})}\end{Bmatrix} \tag{15}$$

where $\phi_\alpha^{(k)}(z_{(j)})\ (\alpha=1,2)$ represents the zigzag function evaluated at the *j*-th interface $(z_i=z_{(j)})$. It should be noted, however, that the strain data measured by the strain rosettes which correspond to the $\mathbf{x}_i$ position do not provide sufficient information to determine either the discrete form $\mathrm{M}_{\alpha i}\ (\alpha=9,10)$ or the continuous form $\mathrm{M}_\alpha\ (\alpha=9,10)$ of the remaining zigzag curvatures. To overcome this difficulty, an accurate estimate of $\mathrm{M}_{\alpha i}\ (\alpha=9,10)$ can be computed by performing a preliminary iFEM analysis using the continuous experimental section strains ($\mathbf{E}$, $\mathbf{K}$, $\mathbf{M}^j$) while ignoring the $\mathbf{G}$ contributions. This preliminary iFEM analysis can produce sufficiently accurate discrete $\mathrm{M}_{\alpha i}\ (\alpha=9,10)$, that are subsequently smoothed by SEA to recover nearly C^1-continuous $\mathrm{M}_\alpha\ (\alpha=9,10)$. Thus, $\mathbf{G}$ is obtained from the four equilibrium equations of RZT that are based on first-order derivatives of $\mathbf{E}$, $\mathbf{K}$, and $\mathrm{M}_\alpha\ (\alpha=7-10)$. As described in Figure 4, this computational strategy results in the continuous form of all experimental section strains $\boldsymbol{\varepsilon}=\begin{bmatrix}\mathbf{E} & \mathbf{K} & \mathbf{M}^j & \mathbf{G}\end{bmatrix}$.

4. Inverse Finite Element Method based on RZT

Following the iFEM methodology of Tessler et al. [37] as a general framework, and accounting for the membrane, bending, zigzag, and transverse-shear deformations of RZT, a weighted least-squares functional $\Phi(\mathbf{u})$ can be defined as

$$\Phi(\mathbf{u})=\sum_{\alpha=1}^{13} w_\alpha\,\varphi_\alpha \tag{16}$$

where $w_\alpha\ (\alpha=1-13)$ are positive valued weighting coefficients associated with the individual section strains and the functional $\varphi_\alpha\ (\alpha=1-13)$ is the least-squares functional of experimental section strains ($\boldsymbol{\varepsilon}$ or $\boldsymbol{\varepsilon}_i$) and kinematic variables $\mathbf{u}$. If the discrete experimental section strains $\boldsymbol{\varepsilon}_i$ are directly used in iFEM analysis, the least-squares functional becomes $\varphi_\alpha=\varphi_\alpha(\mathbf{u},\boldsymbol{\varepsilon}_i)\ (\alpha=1-13)$ and can be defined as the normalized Euclidean norms

$$\varphi_\alpha\equiv\frac{1}{n}\sum_{i=1}^{n}\left[e_\alpha(\mathbf{u})_i-\mathrm{E}_{\alpha i}\right]^2\quad(\alpha=1,2,3) \tag{17a}$$

$$\varphi_\alpha\equiv\frac{(2h)^2}{n}\sum_{i=1}^{n}\left[\kappa_\alpha(\mathbf{u})_i-\mathrm{K}_{\alpha i}\right]^2\quad(\alpha=4,5,6) \tag{17b}$$

$$\varphi_\alpha \equiv \frac{1}{n}\sum_{i=1}^{n}\left[\mu_\alpha^{(k)}(\mathbf{u})_i - \mathrm{M}_{\alpha i}^{j})\right]^2 \quad (\alpha = 7,8,9) \tag{17c}$$

$$\varphi_\alpha \equiv \frac{1}{n}\sum_{i=1}^{n}\left[\gamma_\alpha(\mathbf{u})_i - \Gamma_{\alpha i}\right]^2 \quad (\alpha = 10,11) \tag{17d}$$

$$\varphi_\alpha \equiv \frac{1}{n}\sum_{i=1}^{n}\left[\eta_\alpha(\mathbf{u})_i - \mathrm{H}_{\alpha i}\right]^2 \quad (\alpha = 12,13) \tag{17e}$$

where $1 < k < N$ and $j = k$ or $(k-1)$. If the raw strain data are smoothed a priori (i.e., using SEA analysis as described in section 3) such that the continuous experimental section strain $\boldsymbol{\varepsilon}$ become available for iFEM analysis, the least-squares functional, denoted as $\varphi_\alpha = \varphi_\alpha(\mathbf{u}, \boldsymbol{\varepsilon})$ $(\alpha = 1-13)$, can be defined in terms of the dimensionless L_2 squared norms given as

$$\varphi_\alpha \equiv \frac{1}{A}\int_A \left[e_\alpha(\mathbf{u}) - \mathrm{E}_\alpha\right]^2 dA \quad (\alpha = 1,2,3) \tag{18a}$$

$$\varphi_\alpha \equiv \frac{(2h)^2}{A}\int_A \left[\kappa_\alpha(\mathbf{u}) - \mathrm{K}_\alpha\right]^2 dA \quad (\alpha = 4,5,6) \tag{18b}$$

$$\varphi_\alpha \equiv \frac{1}{A}\int_A \left[\mu_\alpha^{(k)}(\mathbf{u}) - \mathrm{M}_\alpha^{j})\right]^2 dA \quad (\alpha = 7,8,9) \tag{18c}$$

$$\varphi_\alpha \equiv \frac{1}{A}\int_A \left[\gamma_\alpha(\mathbf{u}) - \Gamma_\alpha\right]^2 dA \quad (\alpha = 10,11) \tag{18d}$$

$$\varphi_\alpha \equiv \frac{1}{A}\int_A \left[\eta_\alpha(\mathbf{u}) - \mathrm{H}_\alpha\right]^2 dA \quad (\alpha = 12,13) \tag{18e}$$

The weighting constants w_α $(\alpha = 1-13)$ in Eq. (16) control the complete coherence between the analytic section strains and their experimentally measured values. Their proper usage is especially critical for the problems involving relatively few locations of strain gauges. When every analytic section strain has a corresponding experimentally measured value ($\boldsymbol{\varepsilon}$ or $\boldsymbol{\varepsilon}_i$), the weighting constants are set as $w_\alpha = 1$ $(\alpha = 1-13)$ for Eqs. (17-18). In the case of a missing experimental strain component, the corresponding weighting constant is set as a small number such as $\lambda = 10^{-5}$, and Eqs. (17-18) take on the reduced form defined by the L_2 squared norms

$$\varphi_\alpha \equiv \frac{1}{A}\int_A \left[e_\alpha(\mathbf{u})\right]^2 dA \quad (\mathrm{w}_\alpha = \lambda),\ (\alpha = 1,2,3) \tag{19a}$$

$$\varphi_\alpha \equiv \frac{(2h)^2}{A}\int_A \left[\kappa_\alpha(\mathbf{u})\right]^2 dA \quad (\mathrm{w}_\alpha = \lambda),\ (\alpha = 4,5,6) \tag{19b}$$

$$\varphi_\alpha \equiv \frac{1}{A}\int_A \left[\mu_\alpha^{(k)}(\mathbf{u})\right]^2 dA \ (\mathrm{w}_\alpha = \lambda),\ (\alpha = 7,8,9) \tag{19c}$$

$$\varphi_\alpha \equiv \frac{1}{A}\int_A \left[\gamma_\alpha(\mathbf{u})\right]^2 dA \quad (\mathrm{w}_\alpha = \lambda),\ (\alpha = 10,11) \tag{19d}$$

$$\varphi_\alpha \equiv \frac{1}{A}\int_A \left[\eta_\alpha(\mathbf{u})\right]^2 dA \quad (\mathrm{w}_\alpha = \lambda),\ (\alpha = 12,13) \tag{19e}$$

Furthermore, the iFEM methodology also permits the use of "strain-less" inverse elements – the type of elements that do not have any experimental section strains. For these "strain-less" elements, all squared norms in Eqs. (19) are multiplied by the small weighting constants $w_\alpha = \lambda = 10^{-5}$ $(\alpha = 1-13)$. Therefore, an iFEM discretization can have very sparse measured strain data, and yet the necessary interpolation connectivity can still be maintained between the elements that have strain-sensor data.

5. The inverse-shell element formulation (i3-RZT)

A three-node triangular inverse-shell element, labeled i3-RZT, is developed on the basis of an improved iFEM algorithm. The inverse-element formulation is derived using the Tessler-Dong interdependent interpolation concept [48, 49]. The key concept originates from the RZT beam-frame formulation, from which constraint equations are devised and imposed to each edge of an unconstrained triangular element. The unconstrained triangular element has six nodes, where each corner node has seven displacement DOF and each mid-side node has three displacement DOF. By applying relevant constant-shear edge constraints [51], the displacement DOF at the mid-nodes are condensed out analytically. The resulting element has nine displacement DOF per node (only corner nodes) including the drilling rotations and artificial zigzag rotations, as shown in Figure 5. Due to the inclusion of drilling rotations, this new element has two beneficial aspects: (1) Singular solutions can be simply avoided when modelling complex shell structures; and (2) the i3-RZT element has less tendency toward shear locking for membrane problems. Furthermore, it is much easier to implement the i3-RZT element than the unconstrained element because each single node has the same number of displacement DOF.

The i3-RZT element is defined in a convenient local Cartesian frame of reference (x,y,z), with its origin $(0,0,0)$ located at the centroid of the mid-plane triangle. With the element nodes referred to the global coordinates (X,Y,Z), suitable transformation matrices defining the local-to-global transformations are readily established in accordance with standard finite element procedures to assemble element matrices into a global system of equations (e.g., refer to [50]).

The (x,y) reference plane of the i3-RZT element can be uniquely defined in terms of bilinear isoparametric shape functions as

$$x(s,t) = (1-s-t)x_1 + s x_2 + t x_3 \tag{20a}$$

$$y(s,t) = (1-s-t)y_1 + s y_2 + t y_3 \tag{20b}$$

where s and t are dimensionless isoparametric coordinates and (x_i, y_i) $(i = 1-3)$ are the local nodal coordinates of the element. This definition is necessary for numerical Gauss integration of any function defined on the element surface.

The membrane displacements u and v are defined in terms of their nodal DOF u_i and v_i and the nodal drilling rotations θ_{zi} as

$$u \equiv \sum_{i=1}^{3} (N_i u_i + L_i \theta_{zi}) \tag{21a}$$

$$v \equiv \sum_{i=1}^{3} (N_i v_i - M_i \theta_{zi}) \tag{21b}$$

with N_i and $\{L_i,\ M_i\}$ denoting, respectively, the linear and quadratic interpolation functions that are expressed in terms of the three area-parametric coordinates of the triangle. Note that the quadratic functions L_i and M_i ensure the requisite interaction between the hierarchical drilling rotation DOF and the membrane displacements of the element.

The transverse deflection w, two bending rotations θ_α $(\alpha = 1,2)$, and two zigzag rotations ψ_α $(\alpha = 1,2)$ are interpolated as follows

$$w \equiv \sum_{i=1}^{3} [N_i w_i - L_i(\theta_{xi} - \psi_{xi}) + M_i(\theta_{yi} - \psi_{yi})] \tag{22a}$$

$$\theta_1 \equiv \sum_{i=1}^{3} N_i \theta_{yi} \tag{22b}$$

$$\theta_2 \equiv -\sum_{i=1}^{3} N_i \theta_{xi} \tag{22c}$$

$$\psi_1 \equiv \sum_{i=1}^{3} N_i \psi_{yi} \tag{22d}$$

$$\psi_2 \equiv -\sum_{i=1}^{3} N_i \psi_{xi} \tag{22e}$$

This coupled, anisoparametric interpolation strategy was originally developed by Tessler and Hughes [51] for a three-node Mindlin plate element, MIN3, and subsequently used by many authors, e.g., Versino et al. [52], Cerracchio et al. [45]. The explicit forms of these shape functions are given in Appendix A.

Taking the relevant partial derivatives of Eqs. (21) and (22), and then substituting these derivatives into Eqs. (7) and (9), gives rise to explicit definitions of all section strains in terms of the element nodal displacement vector $\mathbf{u}^e$ as

$$\mathbf{e}(\mathbf{u}^e) = \begin{bmatrix} \mathbf{B}_1\mathbf{u}^e & \mathbf{B}_2\mathbf{u}^e & \mathbf{B}_3\mathbf{u}^e \end{bmatrix}^T \tag{23a}$$

$$\boldsymbol{\kappa}(\mathbf{u}^e) = \begin{bmatrix} \mathbf{B}_4\mathbf{u}^e & \mathbf{B}_5\mathbf{u}^e & \mathbf{B}_6\mathbf{u}^e \end{bmatrix}^T \tag{23b}$$

$$\boldsymbol{\mu}^{(k)}(\mathbf{u}^e) = \begin{bmatrix} \phi_1^{(k)}\mathbf{B}_7\mathbf{u}^e & \phi_2^{(k)}\mathbf{B}_8\mathbf{u}^e & \mathbf{H}_\phi^{(k)}\mathbf{B}_9\mathbf{u}^e \end{bmatrix}^T \tag{23c}$$

$$\boldsymbol{\gamma}(\mathbf{u}^e) = \begin{bmatrix} \mathbf{B}_{10}\mathbf{u}^e & \mathbf{B}_{11}\mathbf{u}^e \end{bmatrix}^T \tag{23d}$$

$$\boldsymbol{\eta}(\mathbf{u}^e) = \begin{bmatrix} \mathbf{B}_{12}\mathbf{u}^e & \mathbf{B}_{13}\mathbf{u}^e \end{bmatrix}^T \tag{23e}$$

where

$$\mathbf{H}_{\phi}^{(k)} = [\phi_1^{(k)} \quad \phi_2^{(k)}] \tag{23f}$$

$$\mathbf{u}^e = \begin{bmatrix} \mathbf{u}_1^e & \mathbf{u}_2^e & \mathbf{u}_3^e \end{bmatrix}^T \tag{23g}$$

$$\mathbf{u}_i^e = \begin{bmatrix} u_i & v_i & w_i & \theta_{xi} & \theta_{yi} & \theta_{zi} & \psi_{xi} & \psi_{yi} & \psi_{zi} \end{bmatrix}^T \quad (i = 1-3) \tag{23h}$$

and the matrices $\mathbf{B}_\alpha$ $(\alpha = 1-13)$ contain derivatives of the shape functions (refer to Appendix B).

Pursuing the procedure in section 3, which enables an accurate computation of continuously distributed experimental section strains $\boldsymbol{\varepsilon}$ and then by substituting Eqs. (23a-e) into Eqs. (16) and (18), results in the element weighted least-squares functional of the form

$$\Phi_e(\mathbf{u}^e) = \sum_{\alpha=1}^{13} w_\alpha \varphi_\alpha(\mathbf{u}^e, \boldsymbol{\varepsilon}) \tag{24}$$

By virtue of these assumptions, all strain compatibility relations are explicitly satisfied so that Eq. (24) can be minimized with respect to the nodal displacement DOF $\mathbf{u}^e$ giving rise to

$$\frac{\partial \Phi_e(\mathbf{u}^e)}{\partial \mathbf{u}^e} = \boldsymbol{\Gamma}^e \mathbf{u}^e - \boldsymbol{\varepsilon}^e = 0 \tag{25a}$$

or simply

$$\boldsymbol{\Gamma}^e \mathbf{u}^e = \boldsymbol{\varepsilon}^e \tag{25b}$$

where $\boldsymbol{\Gamma}^e$ is the element left-hand-side square matrix; $\boldsymbol{\varepsilon}^e$ is the element right-hand-side vector, which is a function of the measured strain values; and $\mathbf{u}^e$ is the nodal displacement vector of the element.

The $\boldsymbol{\varepsilon}^e$ vector is a function of the number of strain sensors within the element as well as the measured section-strain values, and is given by

$$\boldsymbol{\varepsilon}^e = \sum_{\alpha=1}^{13} w_\alpha \mathbf{f}_\alpha^e \tag{26a}$$

where $\mathbf{f}_\alpha^e$ $(\alpha = 1-13)$ vectors denote the contribution of each experimental section strain component and can be explicitly written in terms of experimental section strains as

$$\mathbf{f}_\alpha^e = \frac{1}{A_e} \int_{A_e} \mathbf{B}_\alpha^T \mathrm{E}_\alpha dxdy \quad (\alpha = 1-3) \tag{26b}$$

$$\mathbf{f}_\alpha^e = \frac{(2h)^2}{A_e} \int_{A_e} \mathbf{B}_\alpha^T \mathrm{K}_\alpha dxdy \quad (\alpha = 4-6) \tag{26c}$$

$$\mathbf{f}_7^e = \frac{\phi_1^{(k)}}{A_e} \int_{A_e} \mathbf{B}_7^T \mathrm{M}_7^j dxdy \tag{26d}$$

$$\mathbf{f}_8^e = \frac{\phi_2^{(k)}}{A_e}\int_{A_e} \mathbf{B}_8^T \, \mathrm{M}_8^j \, dxdy \tag{26e}$$

$$\mathbf{f}_9^e = \frac{1}{A_e}\int_{A_e} \mathbf{B}_\alpha^T \left(\mathbf{H}_\phi^{(k)}\right)^T \mathrm{M}_9^j \, dxdy \tag{26f}$$

$$\mathbf{f}_\alpha^e = \frac{1}{A_e}\int_{A_e} \mathbf{B}_\alpha^T \, \Gamma_\alpha \, dxdy \quad (\alpha = 10,11) \tag{26g}$$

$$\mathbf{f}_\alpha^e = \frac{1}{A_e}\int_{A_e} \mathbf{B}_\alpha^T \, \mathrm{H}_\alpha \, dxdy \quad (\alpha = 12,13) \tag{26h}$$

The $\mathbf{\Gamma}^e$ matrix combines the contribution of every analytic section strain component and its corresponding weighting constant w_α $(\alpha = 1-13)$ and is given by

$$\mathbf{\Gamma}^e = \sum_{\alpha=1}^{13} w_\alpha \, \mathbf{k}_\alpha^e \tag{27a}$$

where $\mathbf{k}_\alpha^e$ $(\alpha = 1-13)$ matrices denote the contribution of each analytic section strain component and can be explicitly written in terms of the $\mathbf{B}_\alpha$ $(\alpha = 1-13)$ matrices as

$$\mathbf{k}_\alpha^e = \frac{1}{A_e}\int_{A_e} \mathbf{B}_\alpha^T \, \mathbf{B}_\alpha \, dx\, dy \quad (\alpha = 1-3, 10-13) \tag{27b}$$

$$\mathbf{k}_\alpha^e = \frac{(2h)^2}{A_e}\int_{A_e} \mathbf{B}_\alpha^T \, \mathbf{B}_\alpha \, dx\, dy \quad (\alpha = 4-6) \tag{27c}$$

$$\mathbf{k}_7^e = \frac{\left(\phi_1^{(k)}\right)^2}{A_e}\int_{A_e} \mathbf{B}_7^T \, \mathbf{B}_7 \, dx\, dy \tag{27d}$$

$$\mathbf{k}_8^e = \frac{\left(\phi_2^{(k)}\right)^2}{A_e}\int_{A_e} \mathbf{B}_8^T \, \mathbf{B}_8 \, dx\, dy \tag{27e}$$

$$\mathbf{k}_9^e = \frac{1}{A_e}\int_{A_e} \mathbf{B}_9^T \left(\mathbf{H}_\phi^{(k)}\right)^T \mathbf{H}_\phi \, \mathbf{B}_9 \, dx\, dy \tag{27f}$$

Once $\mathbf{\Gamma}^e$ is constructed according to Eqs. (27a-f), three artificial stiffness terms associated with the drilling ψ_{zi} $(i = 1-3)$ DOF must be added to the $\mathbf{\Gamma}^e$ matrix to avoid singular solutions. These terms are cast in a diagonal matrix $\mathbf{\Gamma}_\psi$ given as

$$\mathbf{\Gamma}_\psi = \begin{bmatrix} k_{\psi z}^1 & 0 & 0 \\ 0 & k_{\psi z}^2 & 0 \\ 0 & 0 & k_{\psi z}^3 \end{bmatrix} \tag{28a}$$

with

$$k_{\psi z}^{i} = \lambda \times \min(k_{\psi x}^{i}, k_{\psi y}^{i}) \quad (i = 1,2,3) \tag{28b}$$

where λ is a small positive constant, e.g., $\lambda = 10^{-5}$, and the coefficients $k_{\psi x}^{i}, k_{\psi y}^{i}$ $(i = 1,2,3)$ are diagonal terms of the $\mathbf{\Gamma}^{e}$ matrix corresponding to the zigzag (ψ_{xi}, ψ_{yi}) $(i = 1-3)$ DOF. Then, the element equations defined in Eq. (25b) can be rewritten as

$$\begin{bmatrix} \mathbf{\Gamma}_{v} & \mathbf{0} \\ \mathbf{0} & \mathbf{\Gamma}_{\psi} \end{bmatrix} \begin{bmatrix} \mathbf{v} \\ \boldsymbol{\psi}_{z} \end{bmatrix} = \begin{bmatrix} \mathbf{f}_{v} \\ \mathbf{0} \end{bmatrix} \tag{28c}$$

where the $\boldsymbol{\psi}_{z}$ vector contains the drilling zigzag DOF, the $\mathbf{v}$ vector represents all other DOF of the i3-RZT element, the $\mathbf{\Gamma}_{v}$ matrix and $\mathbf{f}_{v}$ vector are the sub-elements associated with the $\mathbf{v}$ vector.

Once the element matrix equations are established in their global (system) coordinate system, the element contributions to the global equations of the discretized structure can be constructed via the usual element-assembly operator $\overset{nel}{\underset{e=1}{\Omega}}$ giving rise to the global equations

$$\mathbf{A}\mathbf{U} = \mathbf{Q} \tag{29a}$$

where

$$\mathbf{A} = \overset{nel}{\underset{e=1}{\Omega}} \left[(\mathbf{T}^{e})^{T} \mathbf{\Gamma}^{e} \mathbf{T}^{e} \right] \tag{29b}$$

$$\mathbf{U} = \overset{nel}{\underset{e=1}{\Omega}} \left[(\mathbf{T}^{e})^{T} \mathbf{u}^{e} \right] \tag{29c}$$

$$\mathbf{Q} = \overset{nel}{\underset{e=1}{\Omega}} \left[(\mathbf{T}^{e})^{T} \boldsymbol{\varepsilon}^{e} \right] \tag{29d}$$

where $\mathbf{T}^{e}$ is the transformation matrix of the nodal DOF of an element from the local to the global coordinate system, $\mathbf{A}$ is the global left-hand-side symmetric matrix which is independent of the measured strain values, $\mathbf{U}$ is the global nodal-displacement vector, and $\mathbf{Q}$ is the global right-hand-side vector, which is a function of the measured strain values. In Eqs. (29b-d), the parameter *nel* stands for the total number of inverse finite elements.

The global left-hand-side matrix $\mathbf{A}$ includes the requisite rigid body modes of the discretized structure, and, hence, it is singular. By prescribing problem-specific displacement boundary conditions, the resulting system of equations can be reduced from Eq. (28a) as

$$\mathbf{A}_{R}\mathbf{U}_{R} = \mathbf{Q}_{R} \tag{29e}$$

where $\mathbf{A}_{R}$ is a positive definite matrix that is always non-singular and invertible. The solution of Eq. (29e) is computationally efficient because $\mathbf{A}_{R}$ remains unchanged for a given distribution of strain sensors, and its inverse should be calculated only once during the real-time monitoring process. However, the right-hand-side vector $\mathbf{Q}_{R}$ is dependent on the discrete strain data obtained from all strain sensors. Hence, this vector needs to be updated at each strain-data acquisition increment. Finally, the matrix–vector

multiplication $\mathbf{A}_R^{-1}\mathbf{Q}_R$ gives rise to the unknown DOF vector $\mathbf{U}_R$, which provides the deformed structural shape corresponding to the given experimental strain data. By using the reconstructed nodal displacements, displacements and strains throughout the structure can readily be calculated. Furthermore, by taking advantage of the constitutive relations that relate stresses to strains allows one to determine the stress distributions across the modeled structure. Finally, to facilitate damage detection as part of the SHM process, suitable failure/damage criteria can be invoked.

6. Example problems and results

A simply supported rectangular plate (laminate) with three different lamina stacking sequences (uniaxial, cross-ply and angle-ply) has been originally analyzed in Tessler et al. [43] by way of closed form solutions of the refined zigzag theory (RZT). The authors obtained superior displacement and stress results in comparison to other well-established plate theories: FSDT and Di Sciuva [54]. Herein, this problem is revisited to validate the accuracy of the present iFEM formulation. Following these plate validation cases, the present iFEM formulation is further validated using a wedge-like shell structure composed of laminated composite and sandwich cross-sections. Detailed distributions of the displacements and stresses are examined for all example problems.

Example 1: As depicted in Figure 6, the plate has the length $\mathrm{a} = 1\ \mathrm{m}$, width $\mathrm{b} = 1\ \mathrm{m}$, and uniform thickness $2\mathrm{h} = 0.2\ \mathrm{m}$. The plate is subjected to a sinusoidal varying transverse pressure, $q(\mathrm{X},\mathrm{Y}) = q_0 \sin(\pi \mathrm{X}/\mathrm{a})\sin(\pi \mathrm{Y}/\mathrm{b})$, where the pressure magnitude is $q_0 = -1\ \mathrm{MPa}$. As presented in Figure 6, the kinematic variables are defined as follows: $\mathrm{U}, \mathrm{V}, \text{and } \mathrm{W}$ represent the translations along the coordinate directions $\mathrm{X}, \mathrm{Y}, \text{and } \mathrm{Z}$, respectively; $\theta_{\mathrm{X}}, \theta_{\mathrm{Y}}$ and $\psi_{\mathrm{X}}, \psi_{\mathrm{Y}}$ represent bending and zigzag rotations around the positive $\mathrm{X} \text{ and } \mathrm{Y}$ directions, respectively. The four edges of the plate are simply supported and the following kinematic boundary conditions satisfy the simply supported boundary condition of the plate: For cross-ply and uniaxial laminates, the kinematic boundary conditions along $\mathrm{X} = 0$ and $\mathrm{X} = \mathrm{a}$ are

$$\mathrm{V} = \mathrm{W} = \theta_{\mathrm{X}} = \psi_{\mathrm{X}} = 0 \tag{30a}$$

and along $\mathrm{Y} = 0$ and $\mathrm{Y} = \mathrm{b}$ are

$$\mathrm{U} = \mathrm{W} = \theta_{\mathrm{Y}} = \psi_{\mathrm{Y}} = 0 \tag{30b}$$

For angle-ply laminates, the kinematic boundary conditions along $\mathrm{X} = 0$ and $\mathrm{X} = \mathrm{a}$ are

$$\mathrm{U} = \mathrm{W} = \theta_{\mathrm{X}} = \psi_{\mathrm{X}} = 0 \tag{31a}$$

and along $\mathrm{Y} = 0$ and $\mathrm{Y} = \mathrm{b}$ are

$$\mathrm{V} = \mathrm{W} = \theta_{\mathrm{Y}} = \psi_{\mathrm{Y}} = 0 \tag{31b}$$

Three different laminates (I, II, III) are considered to represent relatively thick laminated composite and sandwich plates with a span-to-thickness ratio of $\mathrm{a}/2\mathrm{h} = \mathrm{b}/2\mathrm{h} = 5$. Laminate I is a two-layer, cross-ply carbon-epoxy laminate. Laminate II is a three-layer sandwich laminate with uniaxial carbon-epoxy face sheets and a thick, closed cell polyvinyl chloride (PVC) core, where PVC is represented as an isotropic material. Laminate III is a five-layer, angle-ply sandwich laminate with carbon-epoxy face sheets and a thick PVC core. The mechanical material properties and the stacking sequences of the laminates are listed

in Tables 1-2, respectively.

To establish an accurate reference solution, a convergence study was first carried out using direct RZT-based FEM analyses utilizing an in-house FEM code. The finest mesh consisted of 10,000 uniformly distributed triangular elements that possessed 35,707 DOF. For the three laminates (I, II, III) considered in the study, comparisons of the normalized central deflection are summarized in Table 3; where the normalization factor of $10^2 D_{11} / q_0 \mathrm{a}^4$ is used, with D_{11} denoting the bending stiffness coefficient. These results clearly demonstrate that the RZT reference FEM solutions are in close agreement with the corresponding exact solutions according to RZT [43]. Subsequently, the RZT-FEM reference solutions are used to provide the simulated strain-sensor strains. In addition, the reference solutions for the displacements and stresses in Tables 4-5 will be used to assess the accuracy of the iFEM predictions for these problems.

In the present iFEM analysis, the strain rosettes are regularly distributed, and each strain rosette configuration pertains to a discretization with the same number of element subdivisions along the plate edges, $\mathrm{n^e}$. Three strain rosettes are positioned at the centroid of each element: one on the top surface, one on the bottom surface, and one along the interface between the first (bottom) and second material layer. In Figure 7, an example of a strain rosette configuration for the $\mathrm{n^e} = 4$ discretization is shown.

Utilizing the computational procedure described in section 3, the continuous section strains ($\mathbf{E}$, $\mathbf{K}$, $\mathbf{M}^j$, and $\mathbf{G}$) are calculated first. Then i3-RZT is formulated based on the continuous form of the section strains $\boldsymbol{\varepsilon}$. The weighting constants associated with the membrane, bending, and zigzag section strains are given the value of unity, $w_\alpha = 1$ $(\alpha = 1-9)$, whereas the weighting constants corresponding to the transverse-shear section strains are set to be sufficiently small, e.g., $w_\alpha = 10^{-8}$ $(\alpha = 10-13)$. This is because the transverse-shear section strains are commonly several orders of magnitude smaller than the other section strains, thus the corresponding weighting constants must be much smaller than unity, with unity representing the weighting constants on the membrane, bending, and zigzag terms. Consequently, this iFEM analysis is expected to provide close agreement between the membrane, bending and zigzag section strains and their corresponding measured values, and a lesser correlation of the small-valued transverse-shear section strains.

For each laminate (I, II, III), the deflections, bending and zigzag rotations, and von Mises stresses corresponding to the i3-RZT (iFEM) and RZT (FEM) analyses are normalized using the reference solutions summarized in Tables 4-5. These normalized expressions are given as follows

$$\overline{\chi} = \chi \,/\, \left|\chi_{\max}^{\mathrm{FEM}}\right| \quad (\chi = \mathrm{W}, \theta_{\mathrm{X}}, \theta_{\mathrm{Y}}, \psi_{\mathrm{X}}, \psi_{\mathrm{Y}}, \sigma_{\mathrm{v}}) \tag{32}$$

In Tables 6-8, the percent difference results, based on the i3-RZT (iFEM) and RZT (FEM) solutions for the maximum values of the normalized kinematic variables in Eq. (32), are given for various discretization models with the varying number of element subdivisions along the plate edges, $\mathrm{n^e}$. The results demonstrate that i3-RZT (iFEM) provides very accurate response predictions. Even for models which use only a small number of strain sensors, e.g., $\mathrm{n^e} = 2$, the present iFEM formulation gives accurate displacement and rotation predictions that differ from reference values by less than 2.5%. The through-the-thickness distributions are depicted in Figures 8-17 for the in-plane displacements, and normal and transverse-shear stresses, where the quantities are normalized as follows

$$\bar{\mathrm{U}}(0, 0.5\mathrm{b}, \mathrm{Z}) = (10^3 D_{11} / q_0 \mathrm{a}^4)\, \mathrm{U}(0, 0.5\mathrm{b}, \mathrm{Z}) \tag{33a}$$

$$\bar{\sigma}_{XX}(0.55a, 0.6b, Z) = (4h^2 / q_0 a^2)\sigma_{XX}(0.55a, 0.6b, Z) \tag{33b}$$

$$\bar{\tau}_{XZ}(0.11a, 0.2b, Z) = (20h / q_0 a^2)\tau_{XZ}(0.11a, 0.2b, Z) \tag{33c}$$

In the figures, the legends "iFEM ($n^e = 4$)" and "iFEM ($n^e = 8$)" represent the normalized iFEM solutions obtained using strain rosette configurations, $n^e = 4$ and $n^e = 8$, respectively; whereas the legend "Reference" represents the normalized FEM reference solutions. For the uniaxial laminate I, the $\bar{U}$ and $\bar{\sigma}_{XX}$ distributions are accurately computed by the i3-RZT model of the sensor configuration $n^e = 4$, as depicted in Figures 8 and 9. There are slight discrepancies in the $\bar{\tau}_{XZ}$ distributions (Figure 10), where iFEM ($n^e = 8$) is best correlated with the reference solution. Note that all $\bar{\tau}_{XZ}$ stress results are obtained using Cauchy's three-dimensional equilibrium equations. These $\bar{\tau}_{XZ}$ stress distributions are continuous through the thickness of the laminates. For sandwich laminates II and III, the iFEM ($n^e = 4$) predictions for the $\bar{U}$ distributions are in close agreement with their corresponding reference solutions and they exhibit a zigzag distribution through the thickness (Figures 11 and 14). In addition, as depicted in Figures 12 and 15, the $\bar{\sigma}_{XX}$ distributions are also accurately computed using the i3-RZT element, where highly accurate normal stresses are produced at the face sheets. Furthermore, the $\bar{\tau}_{XZ}$ stresses in Figures 13, 16, and 17 demonstrate that the iFEM ($n^e = 4$) model can obtain accurate transverse shear stresses that are virtually indistinguishable from their corresponding reference solutions both in the face sheets and core of the sandwich laminates II and III. These results confirm that the present iFEM formulation is suitable for displacement and stress monitoring of relatively thick laminates ($a/2h = b/2h = 5$), while relying on a relatively small number of strain rosettes.

The contour plots of the variables $\bar{W}$, $\bar{\theta}_X$, $\bar{\theta}_Y$, $\bar{\psi}_X$, $\bar{\psi}_Y$, and $\bar{\sigma}_v$ are compared in Figures 18-23, respectively. For conciseness, only contour plots for laminate III (i.e., the most complex laminate considered in the study) are shown. The iFEM and FEM results for the maximum $\bar{W}$ of laminate III differ only by 0.7% (Figure 18). Similar accuracy is achieved for the maximum values of $\bar{\theta}_X$, $\bar{\theta}_Y$, $\bar{\psi}_X$, and $\bar{\psi}_Y$, where the results differ by less than 1.0% (Figures 19-22). For the maximum value of $\bar{\sigma}_v$ for laminate III, the iFEM and FEM predictions differ from each other by only 0.2% (Figure 23). As can be seen from the figures, the iFEM and FEM contours are graphically indistinguishable.

Example 2: A wedge structure with a hole near one of the clamped ends is analyzed to demonstrate the applicability of i3-RZT (iFEM) to model more complex engineering structures. As depicted in Figure 24, the wedge structure has the overall length of $L_1 = 6$ m, width of $L_2 = 2$ m, and uniform thickness of $2h = 0.2$ m. The wedge structure is composed of panels A and B, each having its own group coordinate system, i.e., $(X_\alpha, Y_\alpha, Z_\alpha)$ (α=A, B). The kinematic variables $(U_\alpha, V_\alpha, W_\alpha)$ (α = A, B) shown in Figure 25 represent the translations along the positive coordinate $(X_\alpha, Y_\alpha, Z_\alpha)$ (α=A, B) directions, respectively, whereas the kinematic variables $(\theta_{X\alpha}, \theta_{Y\alpha})$ (α = A, B) and $(\psi_{X\alpha}, \psi_{Y\alpha})$ (α = A, B) denote bending and zigzag rotations around the positive (X_α, Y_α) (α=A, B) directions, respectively. Both ends of the wedge are clamped, and the clamped boundary conditions along $X_A = X_B = 0$ and $X_A = X_B = 6$ m are specified as

$$U_\alpha = V_\alpha = W_\alpha = \theta_{\beta\alpha} = \psi_{\beta\alpha} = 0 \quad (\alpha = A, B; \beta = X, Y) \tag{34}$$

A body force of $g = 100\,\mathrm{kN/m^3}$ is applied to the wedge structure along the negative Z_A direction (refer to Figure 24.) A five-layer, cross-ply sandwich laminate with carbon-epoxy face sheets and a thick PVC core is considered to represent moderately thin sandwich plates with a span-to-thickness ratio of $L_1/2h = 30$. The laminate stacking sequences are summarized in Table 9.

Initially, a convergence study using RZT- shell FEM analysis was performed to establish an accurate reference solution for this problem. The highest fidelity FEM mesh consisted of 18,802 randomly distributed triangular elements with an edge size of $e^{size} = 0.05\,\mathrm{m}$ and 86,535 DOF (refer to Figure 26.) The results of this reference model are used to compute the simulated strain-sensor strains. For panels A and B, the maximum displacements, von Mises stresses, bending and zigzag rotations obtained from FEM analysis are summarized in Tables 10 and 11. These reference values are then used to assess the accuracy of the iFEM analyses.

Five different iFEM analyses of the wedge structure were performed using five different networks of strain rosettes. Each iFEM analysis refers to a case study number; e.g., the first and third analyses are respectively labeled as iFEM (Case I) and iFEM (Case III). Through the thickness coordinate, three strain rosettes are located at the centroid of each element for all iFEM cases; one on the top surface, one on the bottom surface, and one on the nearest interface to the bottom surface of the laminate. In contrast to Example 1, the discrete section strains obtained from FEM analysis were not subjected to initial smoothing. Instead, they were directly used as input in iFEM (Cases I-V). Using absolute values of the reference solutions summarized in Tables 10 and 11, the displacements, bending and zigzag rotations, and von Mises stresses obtained from both iFEM and FEM analyses are normalized as

$$\bar{\chi}_\alpha = \chi_\alpha \,/\, \left|\chi^{\mathrm{FEM}}_{\alpha,\,\max}\right| \quad (\chi = \mathrm{U,V,W},\theta_{\mathrm{X}},\theta_{\mathrm{Y}},\psi_{\mathrm{X}},\psi_{\mathrm{Y}},\sigma_{\mathrm{v}}) \tag{35}$$

where for panel A, $\alpha = \mathrm{A}$, and for panel B, $\alpha = \mathrm{B}$.

In iFEM (Case I), the i3-RZT discretization is identical to the high-fidelity mesh used in the FEM analysis. The i3-RZT model presented in Figure 27 has 18,802 uniformly distributed triangular elements, each of which has three strain rosettes $(\boldsymbol{\varepsilon}_i^+, \boldsymbol{\varepsilon}_i^-, \boldsymbol{\varepsilon}_i^j)$. In iFEM (Case II), the top-surface, bottom-surface, and *j*-th interface strain rosettes are removed from 13,678 i3-RZT elements, and the resulting i3-RZT mesh has only 5124×3 strain rosettes as shown in Figure 28. A coarser i3-RZT discretization is used in the last three case studies, iFEM (Cases III-V). As depicted in Figure 29, the coarser i3-RZT discretization has 4644 randomly distributed triangular elements with an edge size of $e^{size} = 0.1\,\mathrm{m}$ and 21,861 DOF. In iFEM (Case III), as presented in Figure 30, the i3-RZT model has 4644 inverse-elements each of which has three strain rosettes $(\boldsymbol{\varepsilon}_i^+, \boldsymbol{\varepsilon}_i^-, \boldsymbol{\varepsilon}_i^j)$. In iFEM (Case IV), the top-surface, bottom-surface, and *j*-th interface strain rosettes are removed from 2839 i3-RZT elements, and the resulting i3-RZT mesh has only 1825×3 strain rosettes (refer to Figure 31). In iFEM (Case V), as shown in Figure 32, the i3-RZT model has only 1288 inverse elements that have three strain rosettes $(\boldsymbol{\varepsilon}_i^+, \boldsymbol{\varepsilon}_i^-, \boldsymbol{\varepsilon}_i^j)$, whereas all remaining 3376 elements have no experimental strain data. For an i3-RZT element that has no experimental strain data, the corresponding weighting coefficients are set to 10^{-5}. Moreover, the weighting constants corresponding to the transverse-shear section strains are set to a small value $w_\alpha = 10^{-8}$ $(\alpha = 10,11)$, and $w_\alpha = 10^{-6}$ $(\alpha = 12,13)$ for iFEM (Cases I-V).

The results of iFEM (Cases I through V) are compared to the reference FEM results for the maximum

values of expressions in Eq. (35) for panels A and B in Tables 12 and 13, respectively. The iFEM (Case I) results correlate well with the reference solutions for all the variables. These results demonstrate that the present iFEM formulation is very accurate when using high-fidelity meshes in which all elements have experimental strain measurements. The iFEM (Case II) predictions only differ from the reference FEM solutions by less than 4% for panel A and 2% for panel B. These results confirm the superior membrane-bending coupled predictions of the i3-RZT element, especially considering that a high-fidelity i3-RZT model used only a few elements with experimental strain measurements. The iFEM (Case III) solutions for displacements and rotations are somewhat less accurate, differing from the reference solutions by less than 5.6% and 10.8% for panel A and 1.1% and 5.9% for panel B, respectively. These results demonstrate that even when relatively coarse iFEM/i3-RZT discretizations are used, the shape sensing capability is quite accurate. Moreover, the iFEM (Case III) solutions for von Mises stresses differ from the FEM solutions by approximately 14% for panel A and 15.5% for panel B. Even though these results may still be acceptable for some practical applications, they clearly demonstrate that employing high-fidelity iFEM discretizations should be advantageous for stress calculations requiring sufficiently accurate high-strain gradient data.

The maximum deflections (out-of-plane displacements) shown in Table 10, $\mathrm{W}_{\alpha,\,\max}^{\mathrm{FEM}}$ $(\alpha = \mathrm{A, B})$, are much greater than the maximum in-plane displacements and/or rotations, thus the deformed shape (total deformation) of the wedge structure is mainly caused by the deflections. Hence, the accuracy of monitoring the deflections $\bar{\mathrm{W}}_{\mathrm{A}}$ and $\bar{\mathrm{W}}_{\mathrm{B}}$ is crucial for monitoring total deformation. The iFEM (Case IV) and reference FEM results for $\bar{\mathrm{W}}_{\mathrm{A}}$ and $\bar{\mathrm{W}}_{\mathrm{B}}$ are only 2.3% and 2.0%, and the iFEM (Case V) predictions for $\bar{\mathrm{W}}_{\mathrm{A}}$ and $\bar{\mathrm{W}}_{\mathrm{B}}$ differ from the FEM predictions by only 3.8% and 4.9%, respectively. These results demonstrate that iFEM predictions remain sufficiently accurate even considering a coarse i3-RZT model with the missing strain rosette data in many elements. Also, these results demonstrate the i3-RZT excellent shape-sensing capability, even though Cases IV and V are less accurate in terms of relatively small in-plane displacements and rotations. Furthermore, the iFEM (Cases IV and V) and FEM results for von Mises stresses do not exceed 14.6% and 15.5% for panels A and B, respectively. The accuracy of these results is similar to the iFEM (Case III). Hence, these results demonstrate that even when few elements have strain rosette data sufficiently accurate results can be obtained using iFEM models based on i3-RZT.

In Figures 33-40, contour plots for the normalized quantities in Eq. (35) are compared between iFEM (Case IV) and the FEM reference solutions, noting that iFEM (Case IV) is the most challenging of the examples considered in this study. The compared solutions in Figures 35-37, 39 and 40 are in close agreement and graphically indistinguishable. In Figures 33, 34, and 38 there is generally good agreement even for the models which have many elements that do not have measured strains.

Although relatively coarse iFEM discretizations with a large number of strain rosettes, as in Case V, generally yield satisfactory results, the use of such large numbers of strain rosettes ($1{,}288\times 3$ for Case V) may be impractical. Alternatively, an array of FBG sensors can be used, providing a large number of uniaxial strain measurements along the fiber directions. Thus, the iFEM Cases II, IV, and V, in which only several locations of the wedge are instrumented with strain sensors, are now examined. In these cases, as depicted in Figures 28, 31, and 32, each yellow colored i3-RZT element has an FBG sensor aligned with the X_{α} (α=A, B) axes for panels A and B, respectively. To differentiate these FBG-sensor models from those with strain rosettes, these models are labeled as Cases II-, IV-, and V-FBG. For these models, the weighting constants corresponding to the section strains along Y_{α} (α=A, B) and in the X_{α}-Y_{α} (α=A, B)

planes are set as $w_\alpha = 10^{-8}$ $(\alpha = 10,11)$, since FBG sensors do not provide any strain measurements along these directions.

The iFEM (Case II-, IV-, and V-FBG) and FEM contour plots for the $\bar{W}_A$ and $\bar{W}_B$ deflections and the $\bar{\sigma}_{vA}$ and $\bar{\sigma}_{vB}$ von Mises stresses are compared in Figures 41-46. These results demonstrate that in iFEM (Case II-FBG) the maximum $\bar{W}_A$ and $\bar{W}_B$ displacements are underestimated by about 1.5% and 1.6%, respectively, whereas the maximum von Mises stresses differ from the FEM predictions by 2.7% (see Figures 41 and 42). Moreover, for Cases IV- and V-FBG, the iFEM predictions differ from those of FEM by 5.8% for the maximum deflections, and by 12.6% for the maximum von Mises stresses (refer to Figures 43-46). Furthermore, the iFEM and FEM contour plots compare closely in regions of maximum displacements and stresses. These results clearly demonstrate that the iFEM/i3-RZT methodology produces relatively accurate deformation and stress predictions even when only uniaxial FBG strains are available, thus ensuring the practical aspect of this computational methodology.

Finally, in Figures 47-50, von Mises stresses $\bar{\sigma}_{vA}$ along edges L_1 and L_2 are compared to the FEM reference solutions for Cases II, V, II-FBG, and V-FBG. From these results we conclude that: (1) sufficiently accurate von Mises stresses can be recovered even when uniaxial FBG strain sensors are used in a relatively sparse manner (Figures 47-49), and (2) higher fidelity iFEM discretizations are required to model high-strain gradients in order to obtain improved stresses (Figure 50).

7. Conclusions

An improved iFEM formulation is presented to solve the inverse problem of shape and stress sensing of multilayered composite and sandwich plates/shells that have randomly distributed strain sensors. The plate/shell kinematics are described using RZT plate theory. The formulation is based on minimization of a weighted-least-squares functional that accounts for the complete set of section strains (or strain measures) consistent with RZT plate theory. Based on the present iFEM methodology, laminated composite and sandwich plate/shell structures that involve relatively few strain gauges can be analyzed by utilizing weighting constants. One advantage of the present iFEM methodology is that it can be used for the analysis of thin and moderately thick plate and shell structures because the variational principle accommodates the full transverse-shear deformation of the RZT plate theory. Moreover, the formulation is suitable for C^0-continuous discretization, enabling the development of robust inverse-shell elements for performing shape and stress sensing of complex engineering structures.

A new three-node triangular inverse-shell element (i3-RZT) was developed based on the improved iFEM formulation. The i3-RZT element kinematic field accommodates quadratic interpolation functions that permit a robust drilling DOF implementation that has the advantage of avoiding singular solutions when modeling complex shell structures. The formulation is free from the membrane and shear-locking phenomena. Several numerical studies were performed and demonstrated the computational efficiency, high accuracy, and robustness of i3-RZT discretization with respect to the membrane, bending, and membrane-bending coupled structural responses. The practical utility of iFEM/i3-RZT technology for application to engineering structures has been assessed using relatively low- and high-fidelity discretization strategies.

The effects of sensor locations and number of sensors were also explored. The fact that the formulation requires a set of strain sensors positioned between material layers does not present any implementation

difficulties of this technology since current composites manufacturing methods can readily accommodate embedded sensors. It was also demonstrated that even in the presence of relatively sparse strain data, sufficiently accurate reconstruction of deformed structural shapes and stresses can be achieved for the problems considered herein. Finally, the iFEM/i3-RZT methodology can be readily implemented within any general-purpose finite element software (e.g., NASTRAN, ABAQUS, or ANSYS), thus providing a highly desirable and viable computational tool for real-time structural health monitoring of laminated-composite and sandwich structures used in high-performance aerospace vehicles.

Appendix A

The anisoparametric shape functions interpolating the kinematic variables in Eqs. (21, 22) are defined as

$$L_i = L_i(x,y) = \frac{N_i}{2}\left(b_k N_j - b_j N_k\right) \tag{A.1}$$

$$M_i = M_i(x,y) = \frac{N_i}{2}\left(a_j N_k - a_k N_j\right) \tag{A.2}$$

$$N_i = N_i(x,y) = \frac{A_i}{A_e} = \frac{b_i x + a_i y + c_i}{2A_e} \tag{A.3}$$

with

$$a_i = x_k - x_j;\;\; b_i = y_j - y_k \;\; (i=1,2,3;\;\; j=2,3,1;\;\; k=3,1,2) \tag{A.4}$$

where N_i are linear area-parametric coordinates, L_i and M_i are quadratic shape functions, and A_e is the area of the triangle.

Appendix B

The matrices $\mathbf{B}_\alpha$ $(\alpha = 1-13)$ used in Eqs. (23a-e) contain derivatives of the shape functions and are defined as

$$\mathbf{B}_\alpha = \begin{bmatrix} \mathbf{B}_\alpha^1 & \mathbf{B}_\alpha^2 & \mathbf{B}_\alpha^3 \end{bmatrix} \quad (\alpha = 1-13) \tag{B.1}$$

where

$$\left.\begin{aligned} \mathbf{B}_1^i &= \begin{bmatrix} N_{i,x} & 0 & 0 & 0 & 0 & L_{i,x} & 0 & 0 & 0 \end{bmatrix} \\ \mathbf{B}_2^i &= \begin{bmatrix} N_{i,y} & 0 & 0 & 0 & 0 & -M_{i,x} & 0 & 0 & 0 \end{bmatrix} \\ \mathbf{B}_3^i &= \begin{bmatrix} N_{i,y} & N_{i,x} & 0 & 0 & 0 & L_{i,y} - M_{i,x} & 0 & 0 & 0 \end{bmatrix} \end{aligned}\right\} \; (i=1-3) \tag{B.2}$$

$$\left.\begin{aligned} \mathbf{B}_4^i &= \begin{bmatrix} 0 & 0 & 0 & 0 & N_{i,x} & 0 & 0 & 0 & 0 \end{bmatrix} \\ \mathbf{B}_5^i &= \begin{bmatrix} 0 & 0 & 0 & -N_{i,y} & 0 & 0 & 0 & 0 & 0 \end{bmatrix} \\ \mathbf{B}_6^i &= \begin{bmatrix} 0 & 0 & 0 & -N_{i,x} & N_{i,y} & 0 & 0 & 0 & 0 \end{bmatrix} \end{aligned}\right\} \; (i=1-3) \tag{B.3}$$

$$\left.\begin{aligned}\mathbf{B}_7^i &= \begin{bmatrix}0 & 0 & 0 & 0 & 0 & 0 & 0 & N_{i,x} & 0\end{bmatrix} \\ \mathbf{B}_8^i &= \begin{bmatrix}0 & 0 & 0 & 0 & 0 & 0 & -N_{i,y} & 0 & 0\end{bmatrix}\end{aligned}\right\} \quad (i=1-3) \tag{B.4}$$

$$\mathbf{B}_9^i = \begin{bmatrix}0 & 0 & 0 & 0 & 0 & 0 & 0 & N_{i,y} & 0 \\ 0 & 0 & 0 & 0 & 0 & 0 & -N_{i,x} & 0 & 0\end{bmatrix} \quad (i=1-3) \tag{B.5}$$

$$\left.\begin{aligned}\mathbf{B}_{10}^i &= \begin{bmatrix}0 & 0 & N_{i,x} & -L_{i,x} & M_{i,x}+N_i & 0 & L_{i,x} & -M_{i,x} & 0\end{bmatrix} \\ \mathbf{B}_{11}^i &= \begin{bmatrix}0 & 0 & N_{i,y} & -L_{i,y}-N_i & M_{i,y} & 0 & L_{i,y} & -M_{i,y} & 0\end{bmatrix}\end{aligned}\right\} \quad (i=1-3) \tag{B.6}$$

$$\left.\begin{aligned}\mathbf{B}_{12}^i &= \begin{bmatrix}0 & 0 & N_{i,x} & -L_{i,x} & M_{i,x}+N_i & 0 & L_{i,x} & -M_{i,x}-N_i & 0\end{bmatrix} \\ \mathbf{B}_{13}^i &= \begin{bmatrix}0 & 0 & N_{i,y} & -L_{i,y}-N_i & M_{i,y} & 0 & L_{i,y}+N_i & -M_{i,y} & 0\end{bmatrix}\end{aligned}\right\} \quad (i=1-3) \tag{B.7}$$

Note that N_i, L_i, and M_i are the shape functions of the i3-RZT element, which are explicitly given in Appendix A.

References

[1] Glisic, B., and Inaudi, D., 2008. Fibre optic methods for structural health monitoring. John Wiley & Sons.

[2] Herrmann, A.S., Zahlen, P.C., and Zuardy, I., 2005. Sandwich structures technology in commercial aviation. In Sandwich structures 7: Advancing with sandwich structures and materials (pp. 13-26). Springer Netherlands. In: Proceedings of the 7th international conference on sandwich structures (ICSS-7), Aalborg; 29–31 August 2005. pp. 13–26.

[3] Berggreen, C., Branner, K., Jensen, J.F., and Schultz, J.P., 2007. Application and analysis of sandwich elements in the primary structure of large wind turbine blades. Journal of Sandwich Structures and Materials, 9(6), pp. 525-552.

[4] Lolive, E., Casari, P., and Davies, P., 2005. Loading rate effects on foam cores for marine sandwich structures. In Sandwich structures 7: Advancing with sandwich structures and materials (pp. 895-903). Springer Netherlands. In: Proceedings of the 7th international conference on sandwich structures (ICSS-7), Aalborg; 29–31 August 2005. pp. 895–903.

[5] Zou, Y., Tong, L.P.S.G., and Steven, G.P., 2000. Vibration-based model-dependent damage (delamination) identification and health monitoring for composite structures—a review. Journal of Sound and Vibration, 230(2), pp. 357-378.

[6] McCartney, L.N., 1987. Mechanics of matrix cracking in brittle-matrix fibre-reinforced composites. In Proceedings of the Royal Society of London A: Mathematical, Physical and Engineering Sciences (Vol. 409, No. 1837, pp. 329-350). The Royal Society.

[7] Vadakke, V., and Carlsson, L.A., 2004. Experimental investigation of compression failure of sandwich specimens with face/core debond. Composites Part B: Engineering, 35(6), pp. 583-590.

[8] Bray, D.E., and McBride, D., 1992. Nondestructive testing techniques. NASA STI/Recon Technical Report A, 93.

[9] Gherlone, M., Cerracchio, P., Mattone, M., Di Sciuva, M., and Tessler, A., 2012. Shape sensing of 3D frame structures using an inverse finite element method. International Journal of Solids and Structures, 49(22), pp. 3100-3112.

[10] Tikhonov, A. N., and Arsenin, V. Y., 1977. Solutions of ill-posed problems. Winston, Washington, DC.

[11] Liu, P. L., and Lin, H. T., 1996. Direct identification of non-uniform beams using static strains. International Journal of Solids and Structures, 33(19), pp. 2775-2787.

[12] Maniatty, A. M., and Zabaras, N. J., 1994. Investigation of regularization parameters and error estimating in inverse elasticity problems. International Journal for Numerical Methods in Engineering, 37(6), pp. 1039-1052.

[13] Schnur, D. S., and Zabaras, N., 1990. Finite element solution of two-dimensional inverse elastic problems using spatial smoothing. International Journal for Numerical Methods in Engineering, 30(1), pp. 57-75.

[14] Davis, M. A., Kersey, A. D., Sirkis, J., and Friebele, E. J., 1996. Shape and vibration mode sensing using a fiber optic Bragg grating array. Smart Materials and Structures, 5(6), pp. 759.

[15] Kang, L. H., Kim, D. K., and Han, J. H., 2007. Estimation of dynamic structural displacements using fiber Bragg grating strain sensors. Journal of Sound and Vibration, 305(3), pp. 534-542.

[16] Kim, N. S., and Cho, N. S., 2004. Estimating deflection of a simple beam model using fiber optic Bragg-grating sensors. Experimental Mechanics, 44(4), pp. 433-439.

[17] Ko, W. L., Richards, W. L., and Fleischer, V. T., 2009. Applications of Ko displacement theory to the deformed shape predictions of the doubly-tapered Ikhana Wing. NASA/TP-2009-214652.

[18] Chierichetti, M., 2014. Load and response identification for a nonlinear flexible structure subject to harmonic loads. Journal of Computational and Nonlinear Dynamics, 9(1), pp. 011009.

[19] Derkevorkian, A., Masri, S. F., Alvarenga, J., Boussalis, H., Bakalyar, J., and Richards, W. L., 2013. Strain-based deformation shape-estimation algorithm for control and monitoring applications. AIAA Journal, 51(9), pp. 2231-2240.

[20] Jones, R. T., Bellemore, D. G., Berkoff, T. A., Sirkis, J. S., Davis, M. A., Putnam, M. A., and Kersey, A. D., 1998. Determination of cantilever plate shapes using wavelength division multiplexed fiber Bragg grating sensors and a least-squares strain-fitting algorithm. Smart Materials and Structures, 7(2), pp. 178.

[21] Shkarayev, S., Krashantisa, R., and Tessler, A., 2001. An inverse interpolation method utilizing in-flight strain measurements for determining loads and structural response of aerospace vehicles. In: Proceedings of 3rd International Workshop on Structural Health Monitoring, Stanford, California.

[22] Shkarayev, S., Raman, A., and Tessler, A., 2002. Computational and experimental validation enabling a viable in-flight structural health monitoring technology. In: Proceedings of 1st European Workshop on Structural Health Monitoring, Cachan, Paris, France.

[23] Bogert, P. B., Haugse, E. D., and Gehrki, R. E., 2003. Structural shape identification from experimental strains using a modal transformation technique. In: Proceedings of 44th AIAA/ASME/ASCE/AHS Structures, Structural Dynamics and Materials Conference, Norfolk, Virginia.

[24] Nishio, M., Mizutani, T., and Takeda, N., 2010. Structural shape reconstruction with consideration of the reliability of distributed strain data from a Brillouin-scattering-based optical fiber sensor. Smart Materials and Structures, 19(3), pp. 035011.

[25] Tessler, A., and Spangler, J. L., 2003. A variational principal for reconstruction of elastic deformation of shear deformable plates and shells. NASA TM-2003-212445.

[26] Tessler, A., and Spangler, J. L., 2005. A least-squares variational method for full-field reconstruction of elastic deformations in shear-deformable plates and shells. Computer Methods in Applied Mechanics and Engineering, 194(2), pp. 327-339.

[27] Stoesz, C. W., 2013. Method For Analyzing Strain Data. US 8,515,675 B2.

[28] Tessler, A., and Spangler, J. L., 2004. Inverse FEM for full-field reconstruction of elastic deformations in shear deformable plates and shells. In: Proceedings of 2nd European Workshop on Structural Health Monitoring, Munich, Germany.

[29] Quach, C. C., Vazquez, S. L., Tessler, A., Moore, J. P., Cooper, E. G., and Spangler, J. L., 2005. Structural anomaly detection using fiber optic sensors and inverse finite element method. In: Proceedings of AIAA Guidance, Navigation, and Control Conference and Exhibit, San Francisco, California.

[30] Vazquez, S. L., Tessler, A., Quach, C. C., Cooper, E. G., Parks, J., and Spangler J. L., 2005. Structural health monitoring using high-density fiber optic strain sensor and inverse finite element methods. NASA TM-2005-213761.

[31] Tessler, A., Spangler, J. L., Gherlone M., Mattone M., and Di Sciuva, M., 2012. Deformed shape and stress reconstruction in plate and shell structures undergoing large displacements: application of inverse finite element method using fiber bragg grating strains. In: Proceedings of 10th World Congress on Computational Mechanics, Sao Paulo, Brazil.

[32] Kefal, A., Oterkus, E., Tessler, A., and Spangler, J.L., 2016. A quadrilateral inverse-shell element with drilling degrees of freedom for shape sensing and structural health monitoring. Engineering Science and Technology, an International Journal, 19, pp. 1299-1313.

[33] Cerracchio, P., Gherlone, M., Mattone, M., Di Sciuva, M., and Tessler, A., 2010. Shape sensing of three-dimensional frame structures using the inverse finite element method. In: Proceedings of 5th European Workshop on Structural Health Monitoring, Sorrento, Italy.

[34] Gherlone, M., Cerracchio, P., Mattone, M., Di Sciuva, M., and Tessler, A., 2011. Beam shape sensing using inverse finite element method: theory and experimental validation. In: Proceeding of 8th International Workshop on Structural Health Monitoring, Stanford, CA

[35] Gherlone, M., Cerracchio, P., Mattone, M., Di Sciuva, M., and Tessler, A., 2014. An inverse Finite Element Method for beam shape sensing: theoretical framework and experimental validation. Smart Materials and Structures, 23(4), pp. 045027.

[36] Tessler, A. 2007. Structural analysis methods for structural health management of future aerospace vehicles. Key Engineering Materials, 347, pp. 57-66.

[37] Tessler, A., Spangler, J. L., Gherlone, M., Mattone, M., and Di Sciuva, M., 2011. Real-Time characterization of aerospace structures using onboard strain measurement technologies and inverse finite element method. In: Proceedings of the 8th International Workshop on Structural Health Monitoring, Stanford, California.

[38] Kefal, A., and Oterkus, E., 2017. Shape sensing of aerospace structures by coupling of isogeometric analysis and inverse finite element method. In: Proceedings of the 58th AIAA/ASCE/AHS/ASC Structures, Structural Dynamics and Materials Conference. Grapevine, TX.

[39] Kefal, A., and Oterkus, E., 2015. Structural Health Monitoring of marine structures by using inverse Finite Element Method. Analysis and Design of Marine Structures V, pp. 341.

[40] Kefal, A., and Oterkus, E., 2016. Displacement and stress monitoring of a chemical tanker based on inverse finite element method. Ocean Engineering, 112, pp. 33-46.

[41] Kefal, A., and Oterkus, E., 2016. Displacement and stress monitoring of a Panamax containership using inverse finite element method. Ocean Engineering, 119, pp. 16-29.

[42] Kefal, A., and Oterkus, E., 2017. Shape and stress sensing of offshore structures by using inverse finite element method. Progress in the Analysis and Design of Marine Structures, pp. 141-148.

[43] Tessler, A., Di Sciuva, M., and Gherlone, M., 2010. A consistent refinement of first-order shear deformation theory for laminated composite and sandwich plates using improved zigzag kinematics. Journal of Mechanics of Materials and Structures, 5(2), pp. 341-367.

[44] Cerracchio, P., Gherlone, M., Di Sciuva, M., and Tessler, A., 2013. Shape and stress sensing of multilayered composite and sandwich structures using an inverse Finite Element Method. In: Proceedings of V International Conference on Computational Methods for Coupled Problems in Science and Engineering, Ibiza, Spain.

[45] Cerracchio, P., Gherlone, M., Di Sciuva, M., and Tessler, A., 2015. A novel approach for displacement and stress monitoring of sandwich structures based on the inverse Finite Element Method. Composite Structures, 127, pp. 69-76.

[46] Tessler, A., Riggs, H. R., Freese, C. E., and Cook, G. M., 1998. An improved variational method for finite element stress recovery and a posteriori error estimation. Computer Methods in Applied Mechanics and Engineering, 155(1), pp. 15-30.

[47] Tessler, A., Riggs, H. R., and Dambach, M., 1999. A novel four-node quadrilateral smoothing element for stress enhancement and error estimation. International Journal for Numerical Methods in Engineering, 44(10), pp. 1527-1541.

[48] Tessler, A., and Dong, S.B., 1981. On a hierarchy of conforming Timoshenko beam elements. Computers & Structures, 14(3), pp. 335-344.

[49] Tessler, A., 2000. Comparison of interdependent interpolations for membrane and bending kinematics in shear-deformable shell elements. In: Proceedings of international conference on computational engineering and sciences, Los Angeles, CA.

[50] Bathe, K. J., 2006. Finite element procedures. Klaus-Jurgen Bathe.

[51] Tessler, A., and Hughes, T.J., 1985. A three-node Mindlin plate element with improved transverse shear. Computer Methods in Applied Mechanics and Engineering, 50(1), pp. 71-101.

[52] Versino, D., Gherlone, M., Mattone, M., Di Sciuva, M., and Tessler, A., 2013. C^0 triangular elements based on the Refined Zigzag Theory for multilayer composite and sandwich plates. Composites Part B: Engineering, 44(1), pp .218-230.

[53] Pagano, N.J., 1994. Exact solutions for composite laminates in cylindrical bending. In Mechanics of Composite Materials (pp. 72-85). Springer Netherlands.

[54] Di Sciuva, M., 1984. A refinement of the transverse shear deformation theory for multilayered orthotropic plates. In: Atti del VII Congresso Nazionale AIDAA (Naples, 1983), edited by A. Marchese, ESA, Rome, 1984. Also In: Aerotecnica Missili e Spazio 63 (1984), pp. 84–92.

[55] Beukema, R.P., 2012. Embedding technologies of FBG sensors in composites: Technologies, applications and practical use. In: Proceedings of the 6th European Workshop on Structural Health Monitoring, Dresden, Germany.

Table 1. Mechanical properties of orthotropic material (C) and isotropic material (P).

Lamina material		Young's modulus [GPa]	Poisson's ratio	Shear modulus [GPa]
C	Carbon-epoxy unidirectional composite	$E_1^{(k)} = 157.9$ $E_2^{(k)} = 9.584$ $E_3^{(k)} = 9.584$	$\upsilon_{12}^{(k)} = 0.32$ $\upsilon_{13}^{(k)} = 0.32$ $\upsilon_{23}^{(k)} = 0.49$	$G_{12}^{(k)} = 5.930$ $G_{13}^{(k)} = 5.930$ $G_{23}^{(k)} = 3.227$
P	PVC core	$E^{(k)} = 0.104$	$\upsilon^{(k)} = 0.3$	$G^{(k)} = 0.04$

Table 2. Laminate stacking sequences (lamina sequence is in the positive z-direction).

Laminate		Normalized lamina thickness, $\mathrm{h}^{(k)} / \mathrm{h}$	Lamina materials	Lamina orientation [°]
I	Cross-ply composite	(0.5/0.5)	(C/C)	(0/90)
II	Uniaxial sandwich	(0.1/0.8/0.1)	(C/P/C)	(0/0/0)
III	Angle-ply sandwich	(0.05/0.05/0.8/0.05/0.05)	(C/C/P/C/C)	(30/-45/0/45/-30)

Table 3. Normalized maximum (central) deflection, $\bar{\mathrm{w}} = (10^2 D_{11} / q_0 \mathrm{a}^4)\,\mathrm{W}(0.5\mathrm{a}, 0.5\mathrm{b})$.

Laminate	Normalization factor $(10^2 D_{11} / q_0 \mathrm{a}^4)$	RZT analytic ($\bar{\mathrm{w}}$) (Tessler et al., [43])	FEM ($\bar{\mathrm{w}}$)
I	5617.72	1.219	1.219
II	5173.04	29.785	29.775
III	2448.38	14.105	14.101

Table 4. FEM results for the maximum deflections von Mises stresses of the simply supported plate.

Laminate	W_{max}^{FEM} [m]	$\sigma_{v,\,max}^{FEM}$ [Pa]
I	-2.169×10^{-4}	1.306×10^{7}
II	-5.756×10^{-3}	1.397×10^{6}
III	-5.759×10^{-3}	2.587×10^{7}

Table 5. FEM results for the maximum bending and zigzag rotations of the simply supported plate.

Laminate	$\theta_{X,\,max}^{FEM}$ [rad]	$\theta_{Y,\,max}^{FEM}$ [rad]	$\psi_{X,\,max}^{FEM}$ [rad]	$\psi_{Y,\,max}^{FEM}$ [rad]
I	5.128×10^{-4}	5.128×10^{-4}	5.520×10^{-5}	5.520×10^{-5}
II	4.009×10^{-3}	1.913×10^{-3}	1.415×10^{-2}	1.607×10^{-2}
III	2.732×10^{-3}	1.571×10^{-3}	1.538×10^{-2}	1.652×10^{-2}

Table 6. Comparison of iFEM to FEM results for maximum values of kinematic variables for laminate I.

n^e	Percent difference				
	$\bar{W}$	$\bar{\theta}_X$	$\bar{\theta}_Y$	$\bar{\psi}_X$	$\bar{\psi}_Y$
2	1.75	2.08	2.08	2.10	2.10
4	1.57	0.70	0.70	0.93	0.93
6	0.28	0.16	0.16	0.66	0.66
8	0.15	0.05	0.05	0.26	0.26
10	0.00	0.04	0.04	0.28	0.28

Table 7. Comparison of iFEM to FEM results for maximum values of kinematic variables for laminate II.

n^e	Percent difference				
	$\bar{W}$	$\bar{\theta}_X$	$\bar{\theta}_Y$	$\bar{\psi}_X$	$\bar{\psi}_Y$
2	1.42	2.26	1.67	1.92	2.13
4	0.74	0.78	0.53	0.66	0.72
6	0.08	0.12	0.21	0.08	0.17
8	0.06	0.09	0.02	0.06	0.06
10	0.00	0.05	0.03	0.06	0.04

Table 8. Comparison of iFEM to FEM results for maximum values of kinematic variables for laminate III.

n^e	Percent difference				
	$\bar{W}$	$\bar{\theta}_X$	$\bar{\theta}_Y$	$\bar{\psi}_X$	$\bar{\psi}_Y$
2	1.25	2.00	1.52	1.74	1.90
4	0.74	0.75	0.55	0.66	0.70
6	0.09	0.06	0.07	0.01	0.12
8	0.06	0.11	0.05	0.09	0.08
10	0.01	0.06	0.06	0.08	0.05

Table 9. Wedge laminate stacking sequences (lamina sequence is in the positive z-direction).

Wedge Laminate	Normalized lamina thickness, $h^{(k)}/h$	Lamina materials	Lamina orientation [°]
Cross-ply sandwich	(0.05/0.05/0.8/0.05/0.05)	(C/C/P/C/C)	(0/90/0/90/0)

Table 10. FEM results for the maximum displacements and von Mises stresses of the wedge structure.

α	$U^{FEM}_{\alpha,\max}$ [m]	$V^{FEM}_{\alpha,\max}$ [m]	$W^{FEM}_{\alpha,\max}$ [m]	$\sigma^{FEM}_{v\alpha,\max}$ [Pa]
A	-4.353×10^{-5}	-2.059×10^{-4}	-1.389×10^{-2}	9.874×10^{7}
B	1.101×10^{-4}	8.601×10^{-4}	-1.031×10^{-2}	9.238×10^{7}

Table 11. FEM results for the maximum bending and zigzag rotations of the wedge structure.

α	$\theta^{FEM}_{X\alpha,\max}$ [rad]	$\theta^{FEM}_{Y\alpha,\max}$ [rad]	$\psi^{FEM}_{X\alpha,\max}$ [rad]	$\psi^{FEM}_{Y\alpha,\max}$ [rad]
A	6.119×10^{-3}	1.243×10^{-3}	-1.350×10^{-3}	-7.128×10^{-3}
B	6.084×10^{-3}	1.120×10^{-3}	-2.117×10^{-3}	5.314×10^{-3}

Table 12. Comparison of iFEM (Cases I-V) to FEM results for maximum values of variables for panel A.

Case	Percent difference							
	$\bar{U}_A$	$\bar{V}_A$	$\bar{W}_A$	$\bar{\theta}_{XA}$	$\bar{\theta}_{YA}$	$\bar{\psi}_{XA}$	$\bar{\psi}_{YA}$	$\bar{\sigma}_{vA}$
I	0.0	0.0	0.0	0.0	0.0	0.1	0.0	0.2
II	0.1	0.0	0.0	1.1	3.7	2.8	0.0	0.2

III	5.6	0.8	1.0	0.8	0.8	10.8	1.7	14.0
IV	12.4	22.5	2.3	9.0	3.3	7.6	3.8	14.6
V	18.1	52.2	3.8	19.4	7.7	3.2	4.7	14.5

Table 13. Comparison of iFEM (Cases I-V) to FEM results for maximum values of variables for panel B.

Case	Percent difference							
	$\bar{U}_B$	$\bar{V}_B$	$\bar{W}_B$	$\bar{\theta}_{XB}$	$\bar{\theta}_{YB}$	$\bar{\psi}_{XB}$	$\bar{\psi}_{YB}$	$\bar{\sigma}_{vB}$
I	0.0	0.0	0.0	0.0	0.0	0.0	0.0	0.2
II	0.2	0.3	0.0	1.1	0.1	1.7	0.0	0.2
III	1.1	0.7	1.1	0.8	5.9	5.7	2.4	15.5
IV	3.6	0.3	2.0	9.1	8.5	6.4	5.0	15.5
V	5.1	2.5	4.9	19.5	21.5	8.5	5.8	15.5

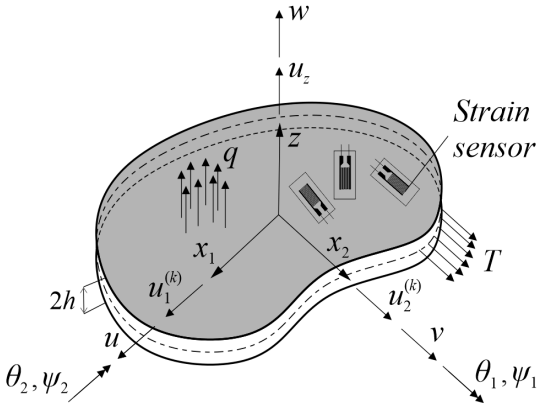

Figure 1. RZT-based iFEM plate notation.

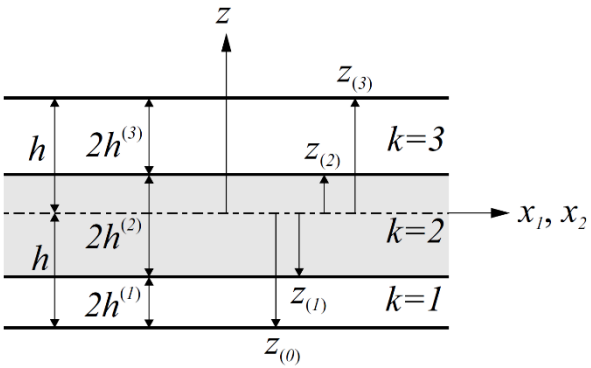

Figure 2. Layer notation for a three-layer laminate.

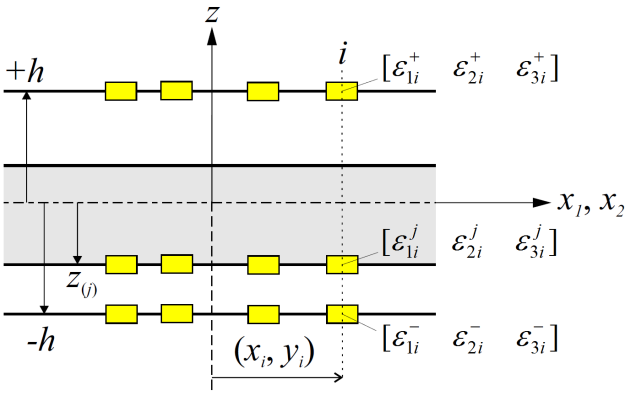

Figure 3. Strain rosettes and experimental surface strain measurements.

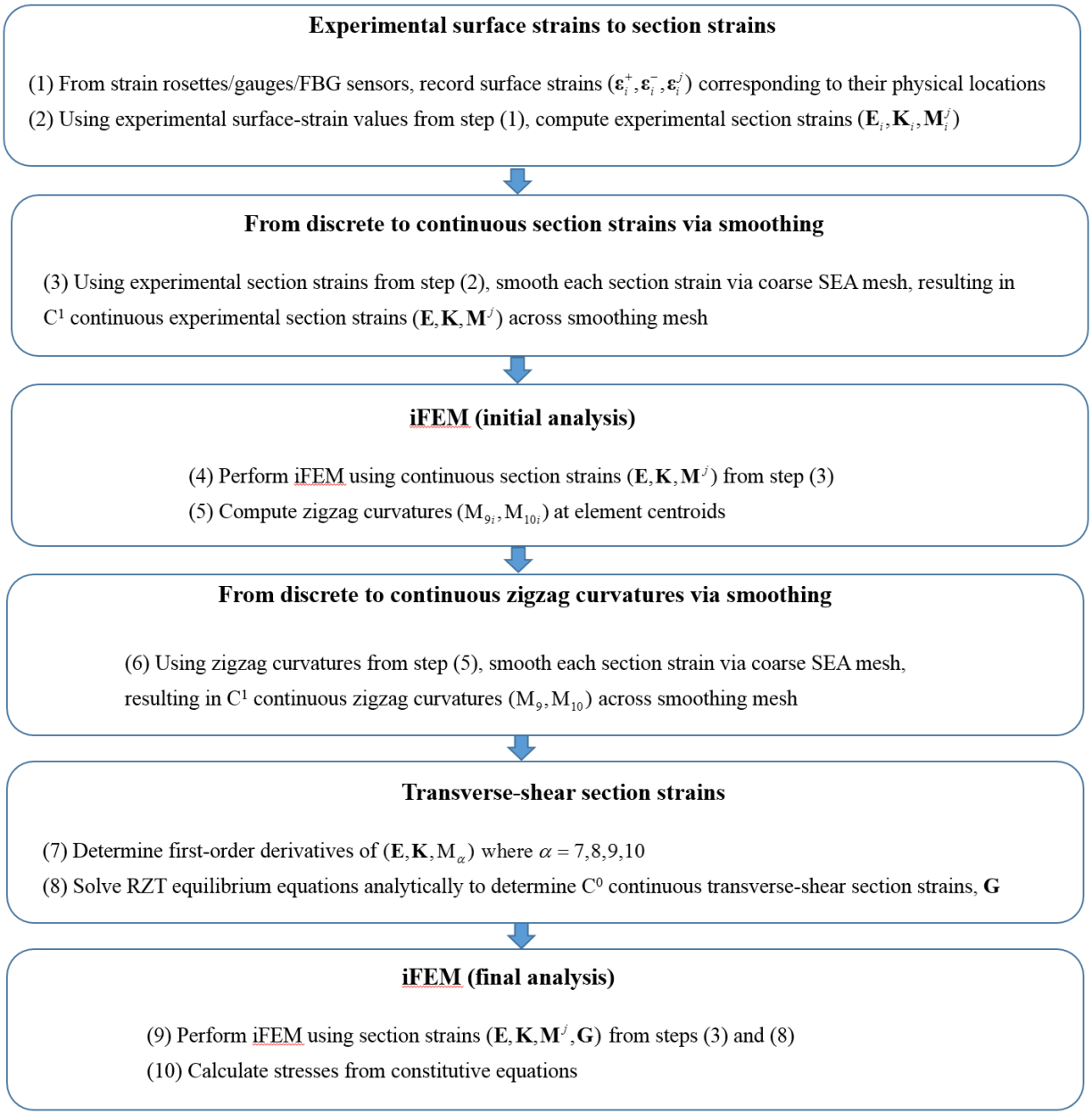

Figure 4. iFEM/SEA computational procedure.

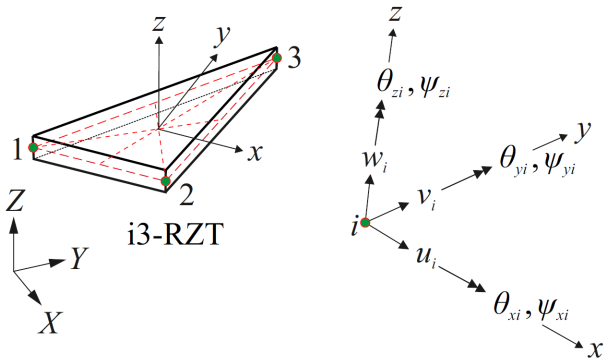

Figure 5. The i3-RZT inverse-shell element and its nodal DOF.

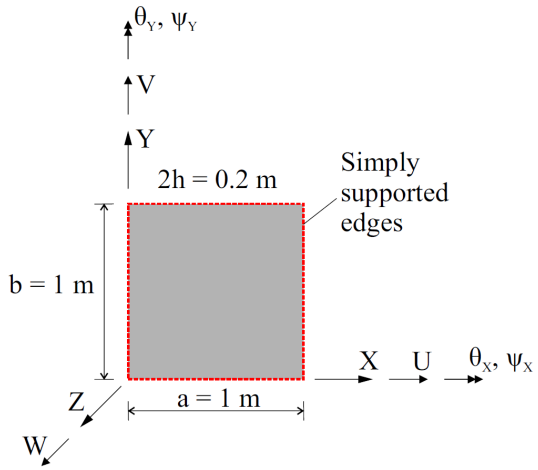

Figure 6. Simply supported plate subjected to sinusoidal varying pressure.

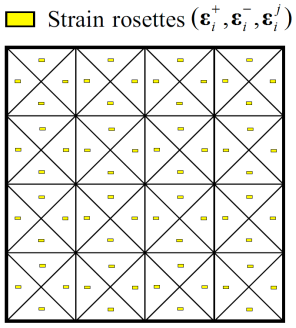

Figure 7. Strain rosette configuration of simply supported plate for discretization $n^e = 4$.

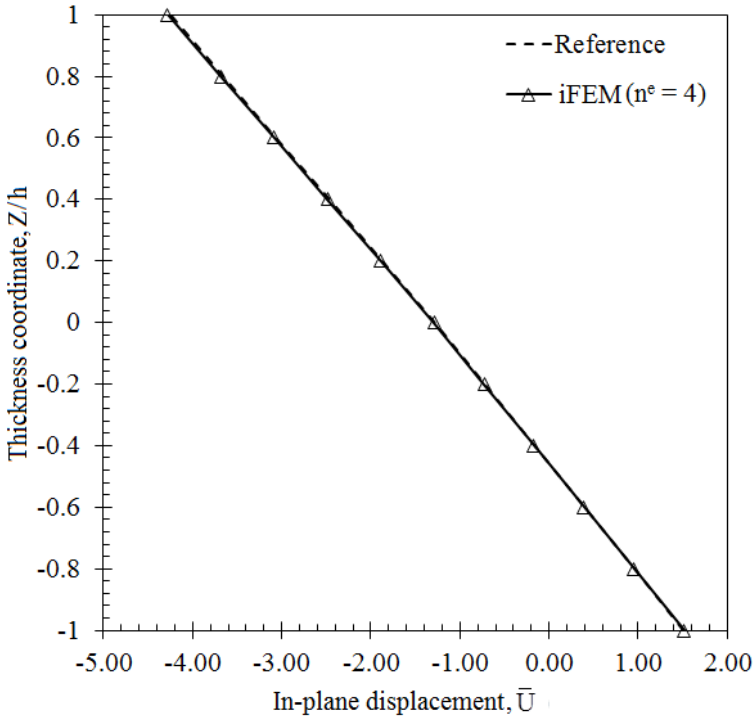

Figure 8. Through-thickness distribution of in-plane displacement $\bar{U}(0, 0.5b, Z)$ for laminate I.

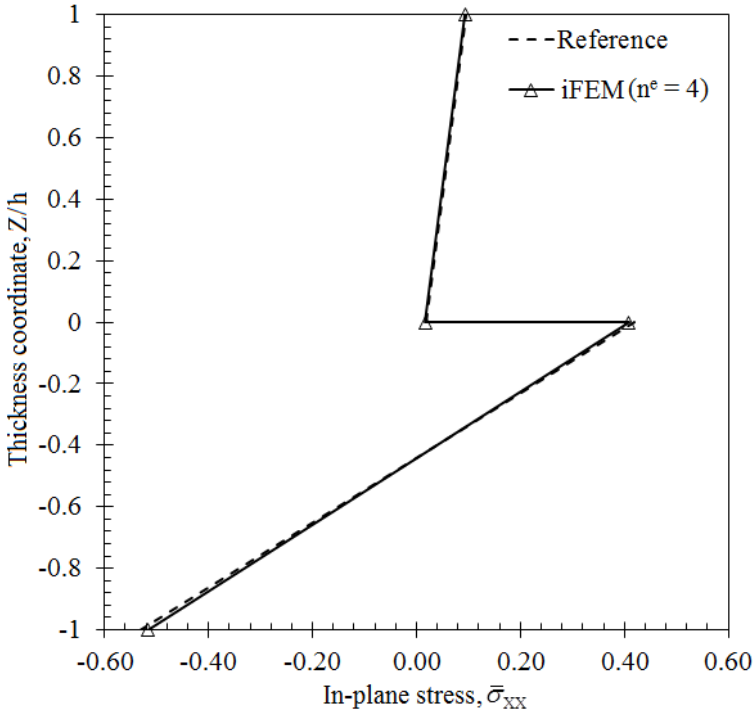

Figure 9. Through-thickness distribution of in-plane stress $\bar{\sigma}_{XX}(0.55a, 0.6b, Z)$ for laminate I.

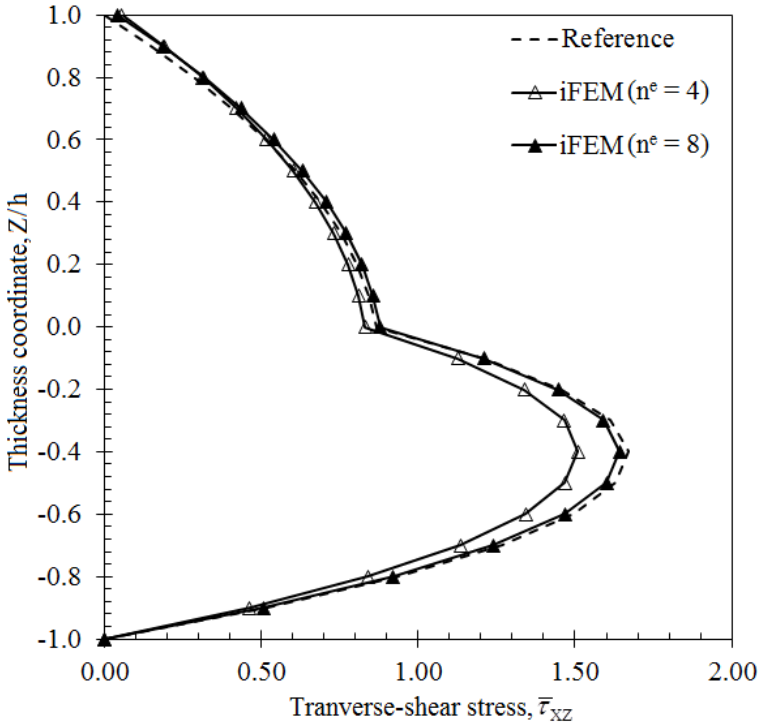

Figure 10. Through-thickness distribution of transverse-shear stress $\bar{\tau}_{XZ}(0.11a, 0.2b, Z)$ for laminate I.

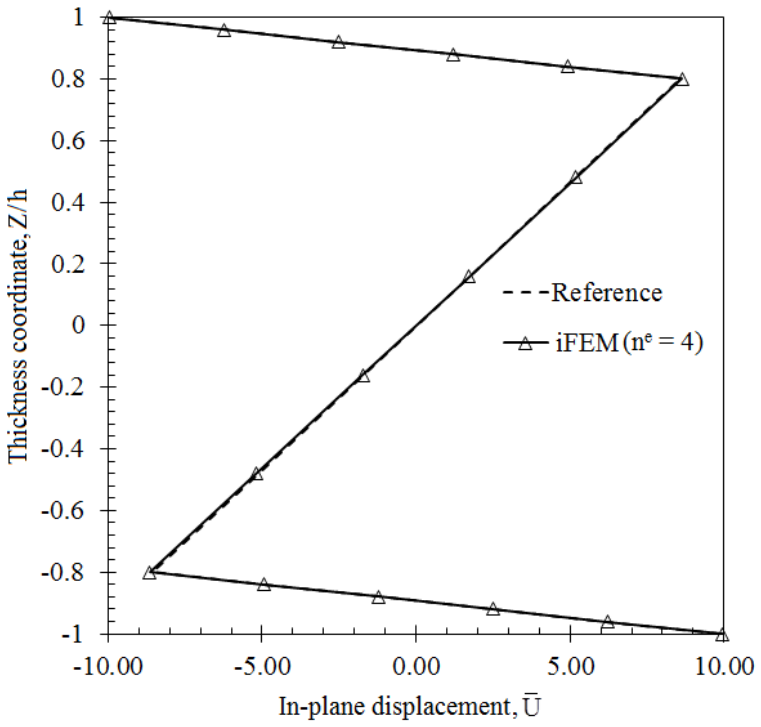

Figure 11. Through-thickness distribution of in-plane displacement $\bar{U}(0, 0.5b, Z)$ for laminate II.

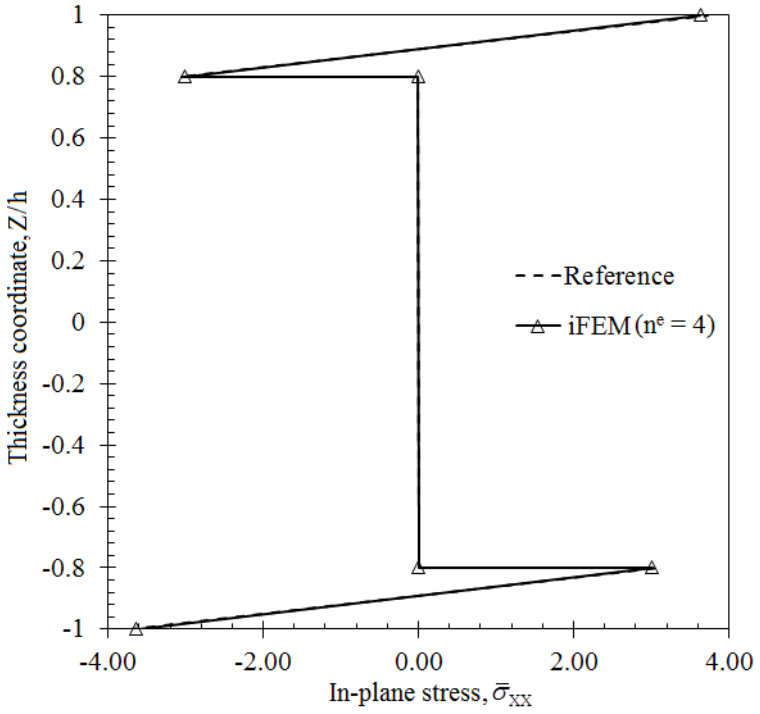

Figure 12. Through-thickness distribution of in-plane stress $\bar{\sigma}_{XX}(0.55a, 0.6b, Z)$ for laminate II.

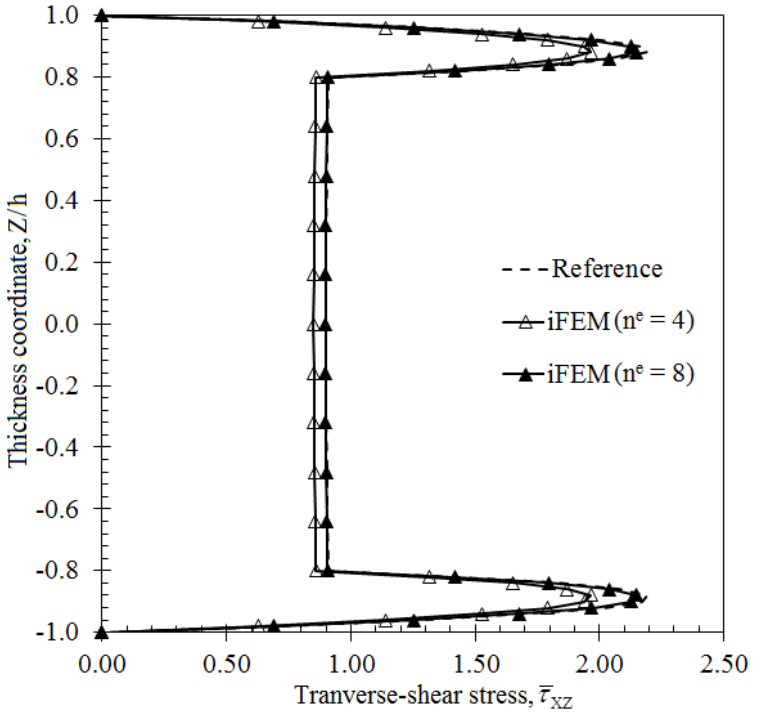

Figure 13. Through-thickness distribution of transverse-shear stress $\bar{\tau}_{XZ}(0.11a, 0.2b, Z)$ for laminate II.

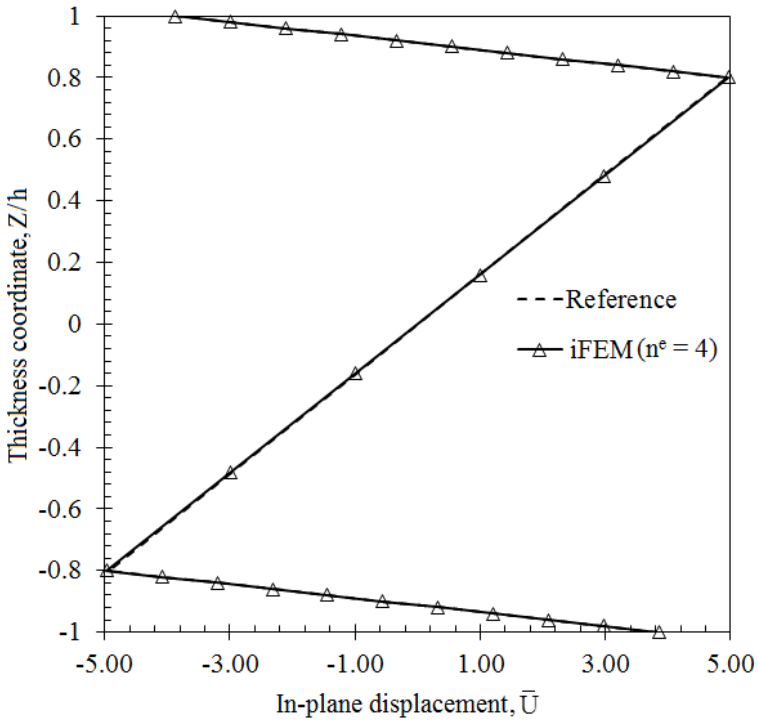

Figure 14. Through-thickness distribution of in-plane displacement $\bar{U}(0, 0.5b, Z)$ for laminate III.

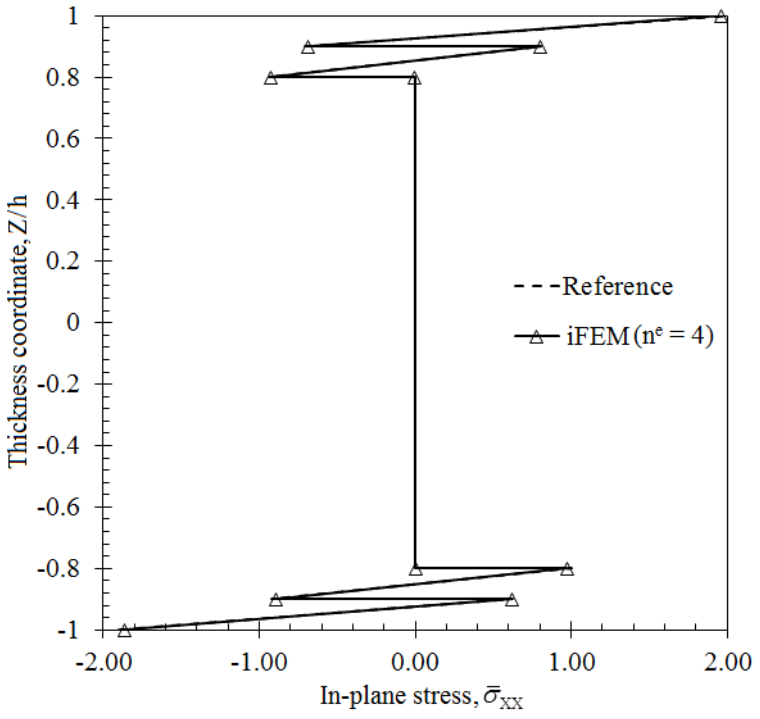

Figure 15. Through-thickness distribution of in-plane stress $\bar{\sigma}_{XX}(0.55a, 0.6b, Z)$ for laminate III.

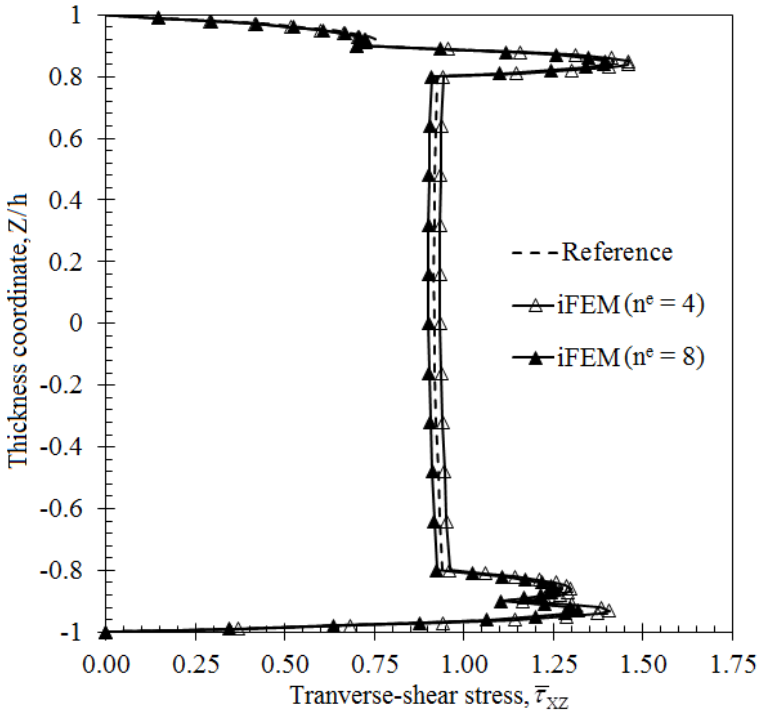

Figure 16. Through-thickness distribution of transverse-shear stress $\bar{\tau}_{XZ}(0.11a, 0.2b, Z)$ for laminate III.

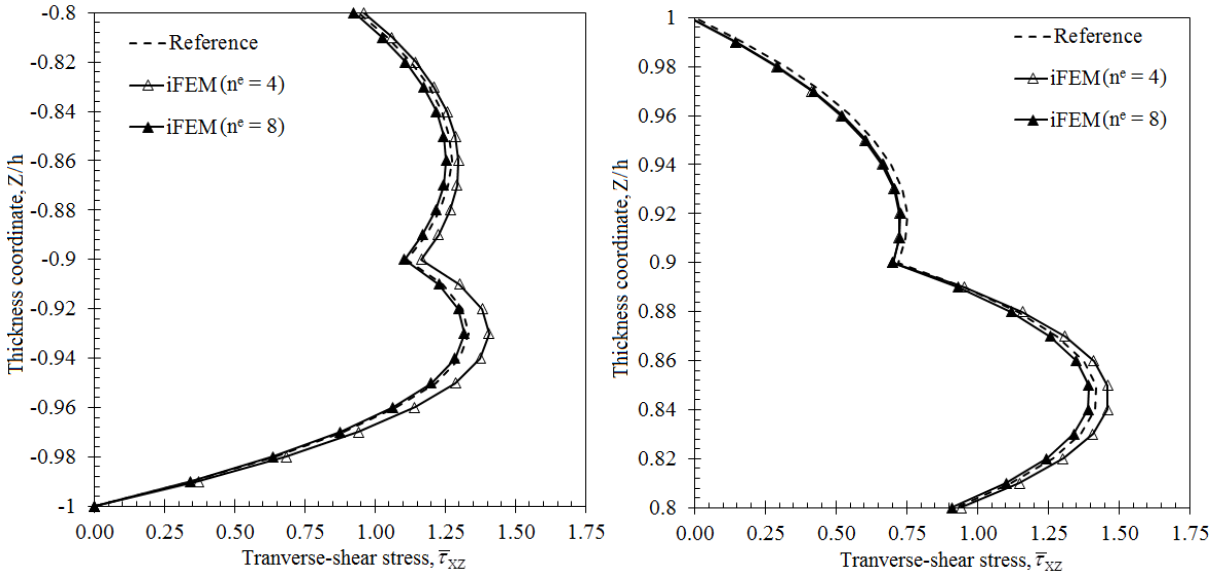

(a) (b)

Figure 17. Close-up views of transverse-shear stresses in Figure 16 in the range of (a) $Z/h \in [-1, -0.8]$ and (b) $Z/h \in [0.8, 1]$.

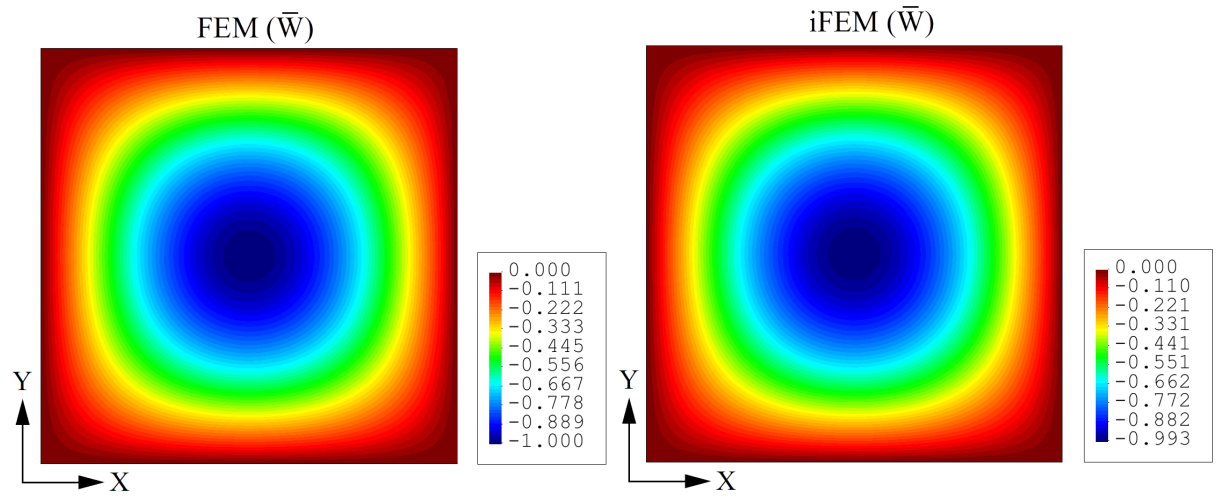

Figure 18. Contour plots of $\bar{W}$ displacement for laminate III: Comparison of high-fidelity FEM and iFEM ($n^e = 4$) results.

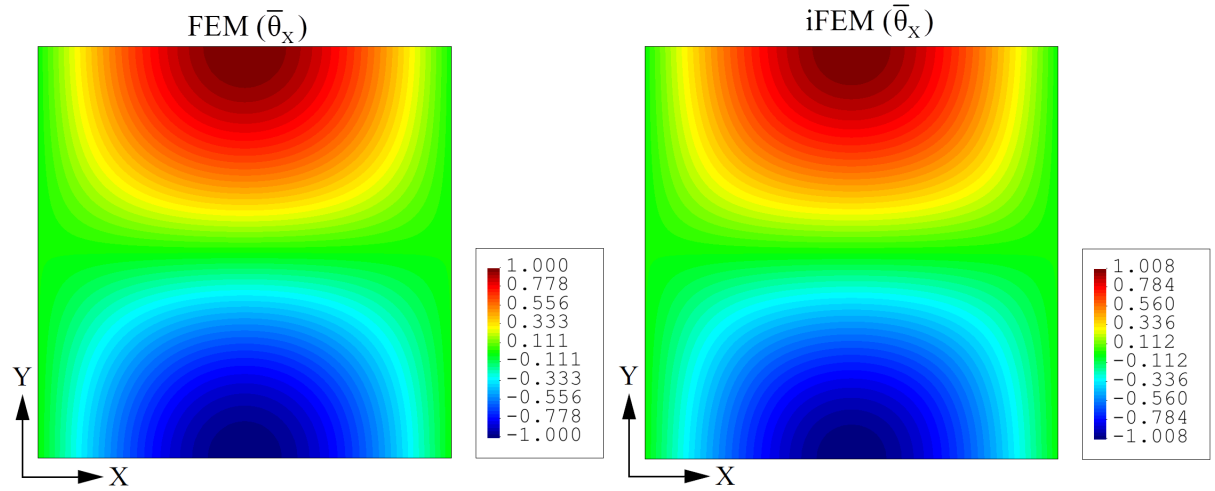

Figure 19. Contour plots of $\bar{\theta}_X$ bending rotation for laminate III: Comparison of high-fidelity FEM and iFEM ($n^e = 4$) results.

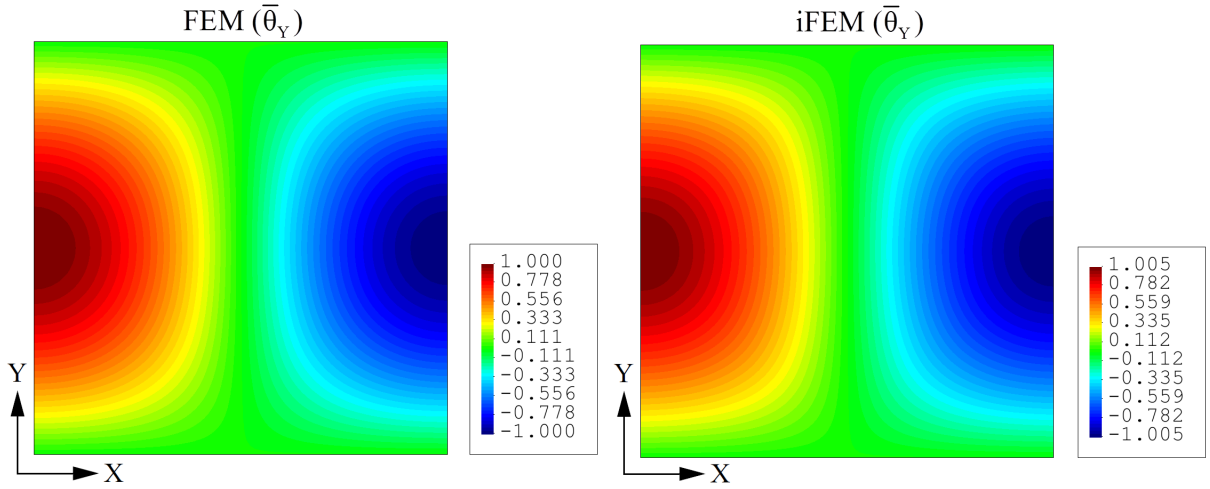

Figure 20. Contour plots of $\bar{\theta}_Y$ bending rotation for laminate III: Comparison of high-fidelity FEM and iFEM ($n^e = 4$) results.

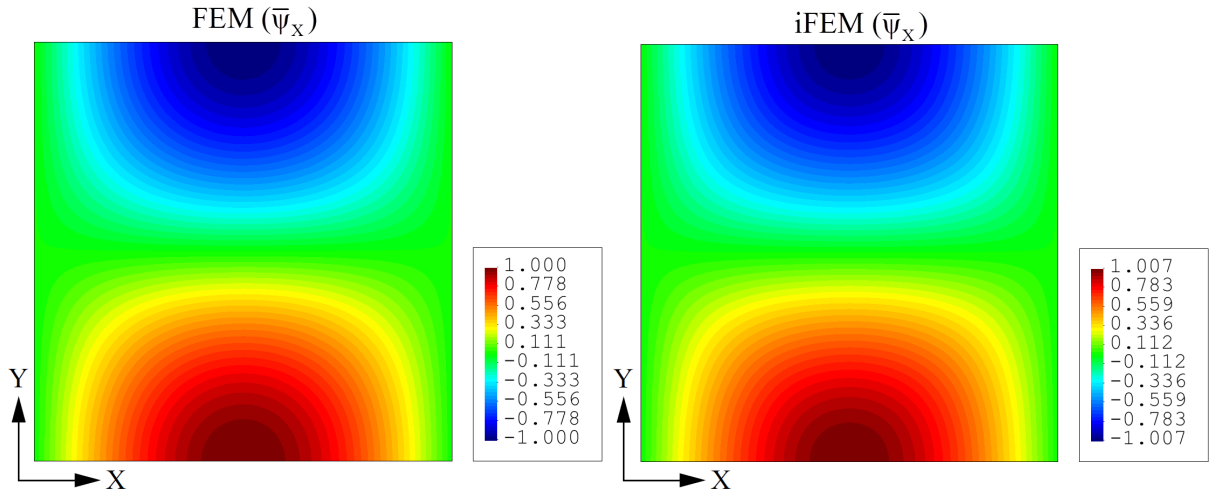

Figure 21. Contour plots of $\bar{\psi}_X$ zigzag rotation for laminate III: Comparison of high-fidelity FEM and iFEM ($n^e = 4$) results.

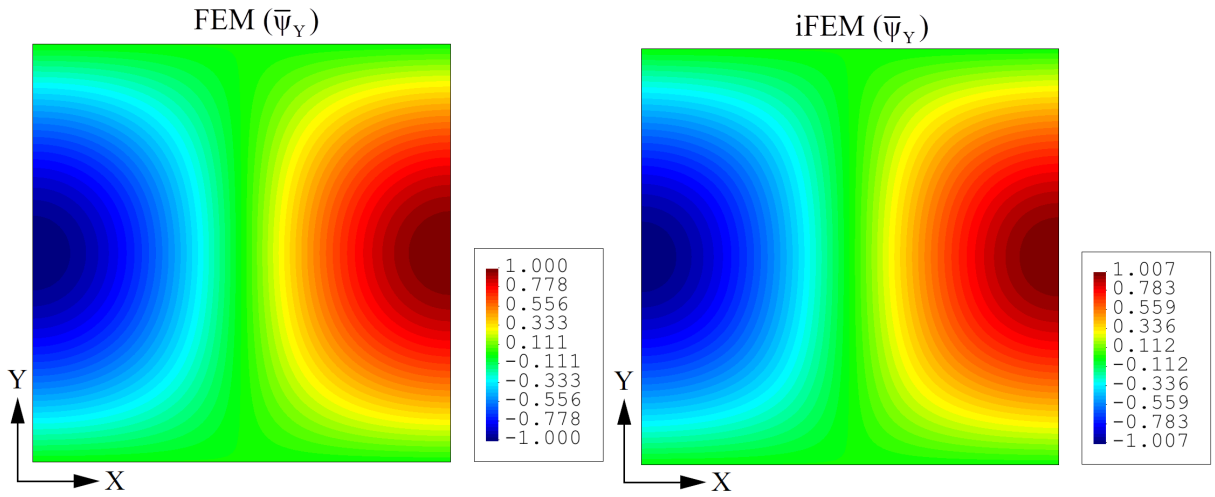

Figure 22. Contour plots of $\bar{\psi}_Y$ zigzag rotation for laminate III: Comparison of high-fidelity FEM and iFEM ($n^e = 4$) results.

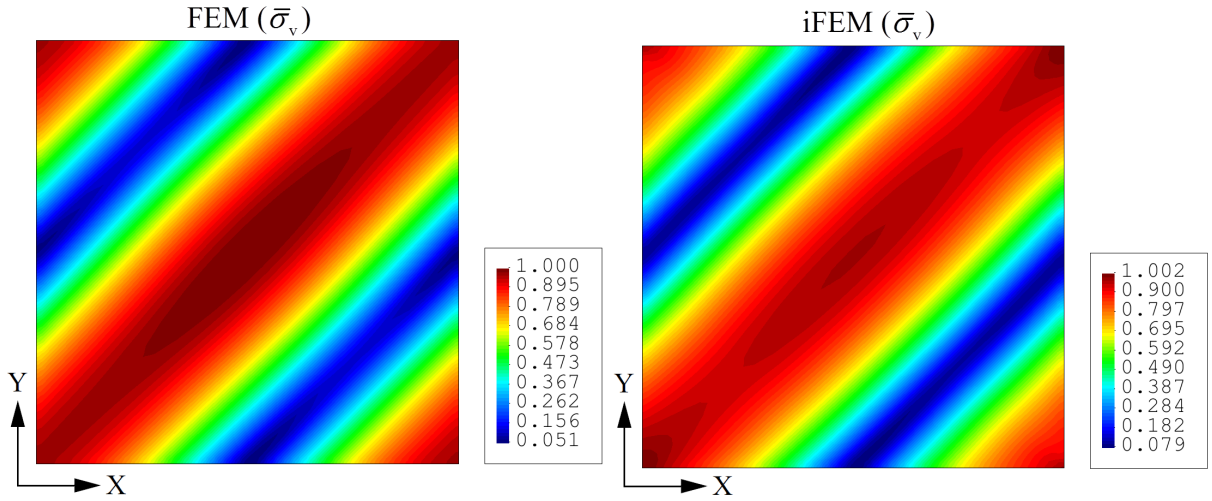

Figure 23. Contour plots of von Mises stress $\bar{\sigma}_v(Z/h=-1)$ of laminate III: Comparison of high-fidelity FEM and iFEM ($n^e = 4$) results.

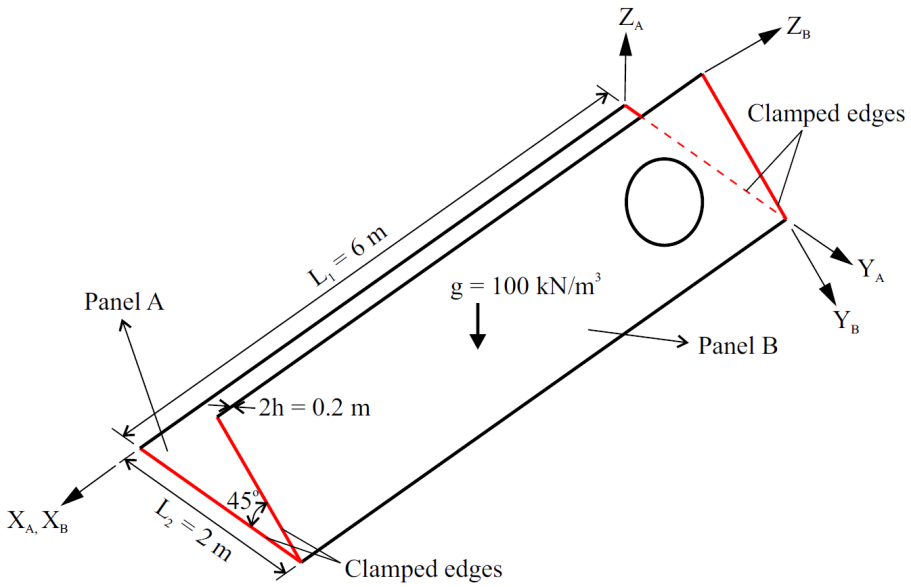

Figure 24. Isometric view of the wedge structure.

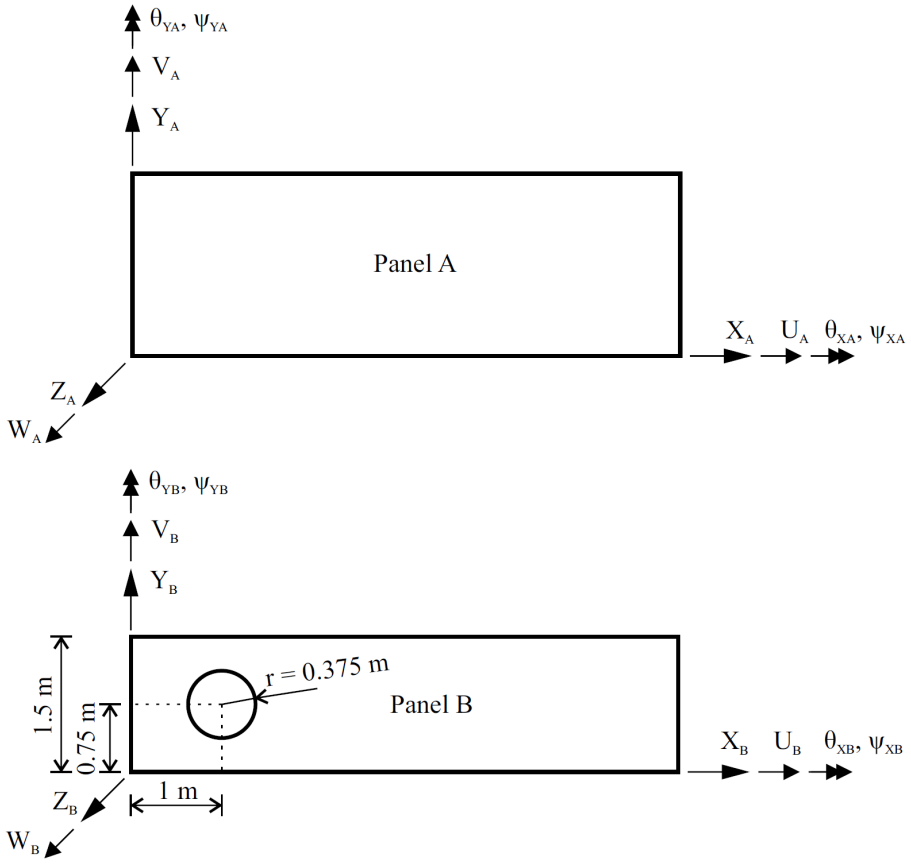

Figure 25. Panels A and B, group coordinate systems, and kinematic variables.

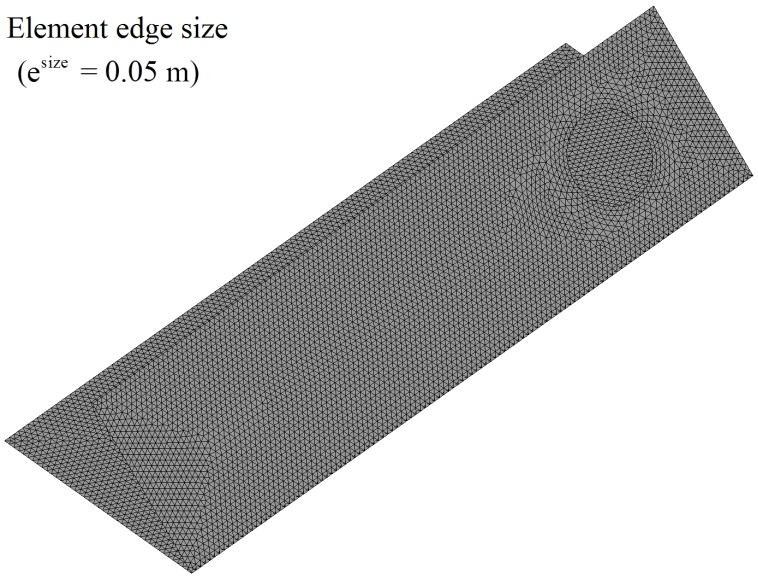

Figure 26. Discretization (18,802 elements) of wedge structure.

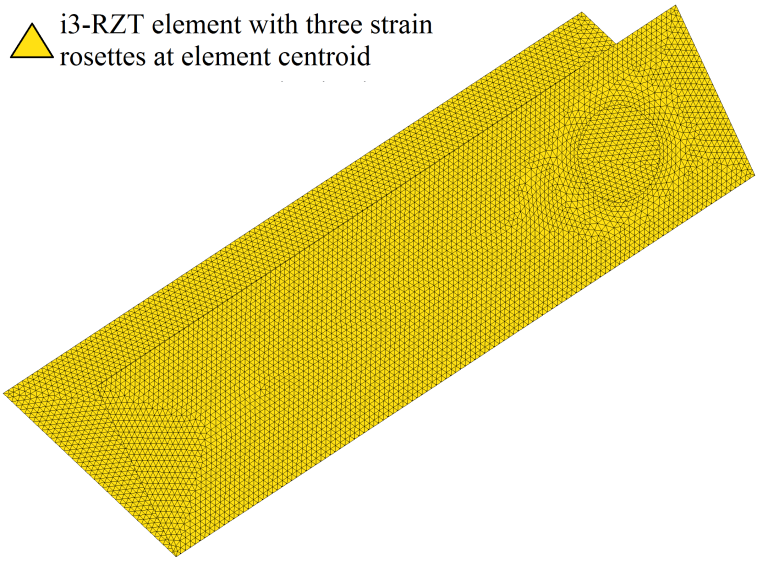

Figure 27. iFEM (Case I) model.

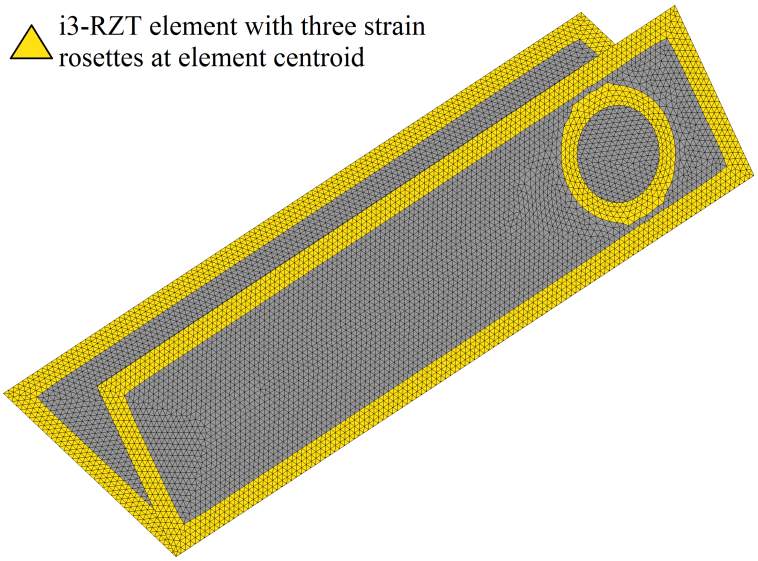

Figure 28. iFEM (Case II) model.

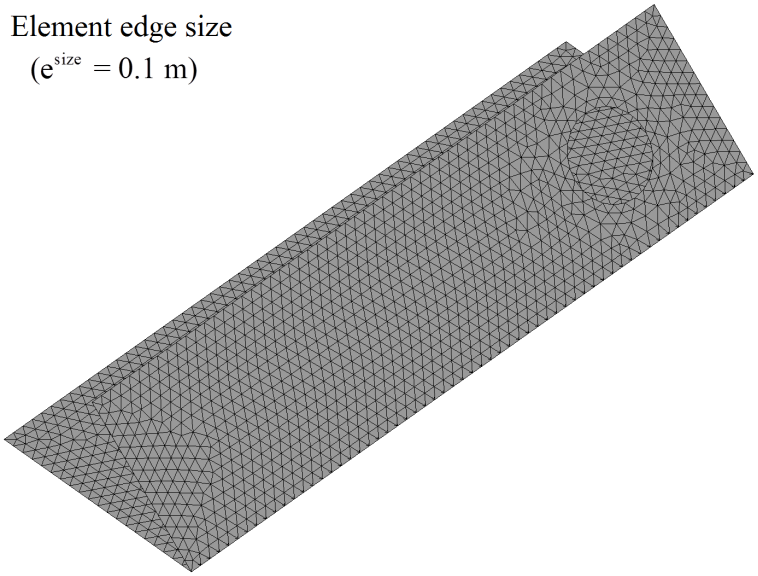

Figure 29. Discretization (4,644 elements) of wedge structure.

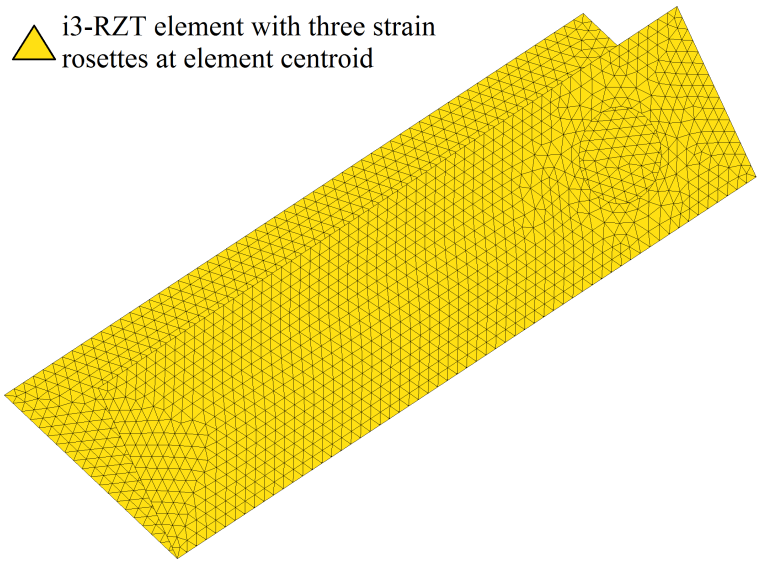

Figure 30. iFEM (Case III) model.

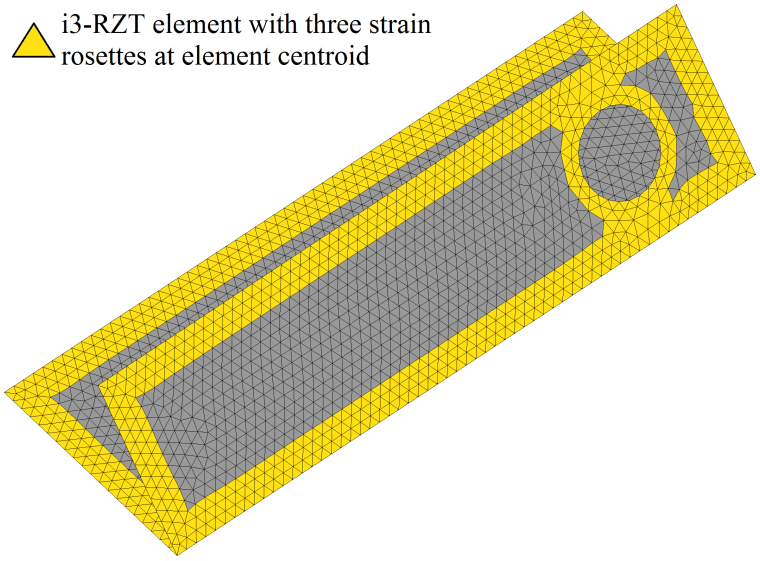

Figure 31. iFEM (Case IV) model.

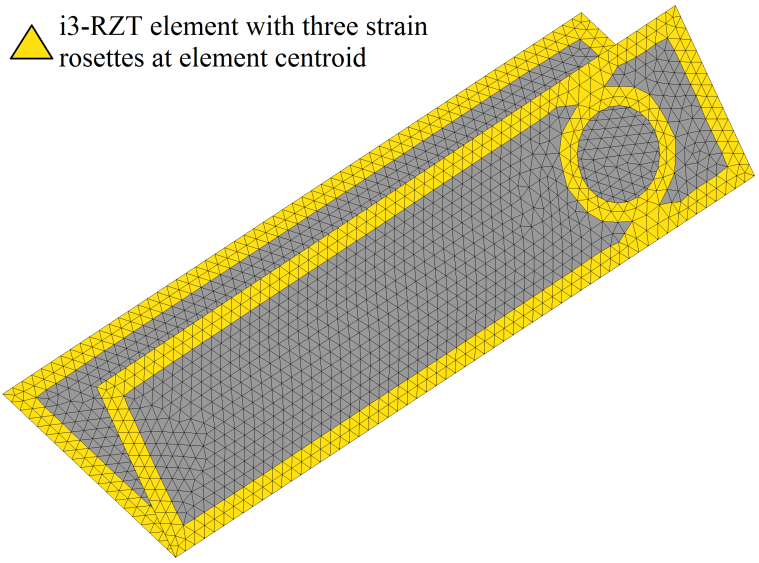

Figure 32. iFEM (Case V) model.

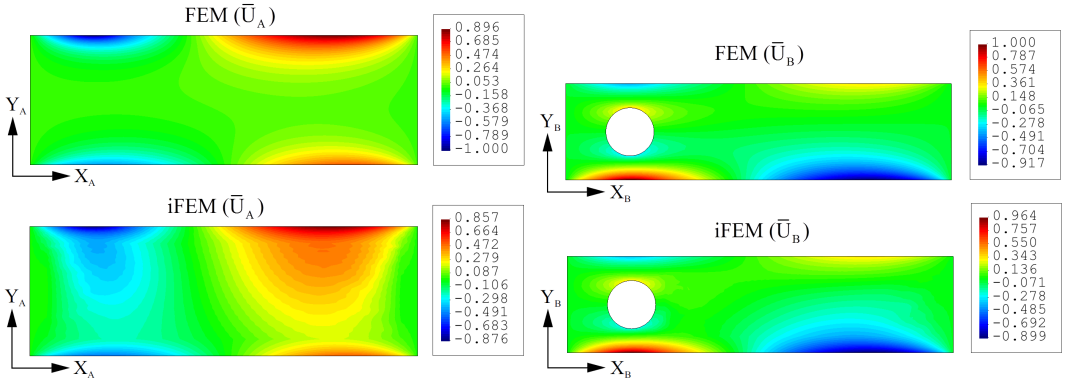

Figure 33. Contour plots of $\bar{U}_A$ and $\bar{U}_B$ displacements for panels A and B: Comparison of high-fidelity FEM and iFEM (Case IV) results.

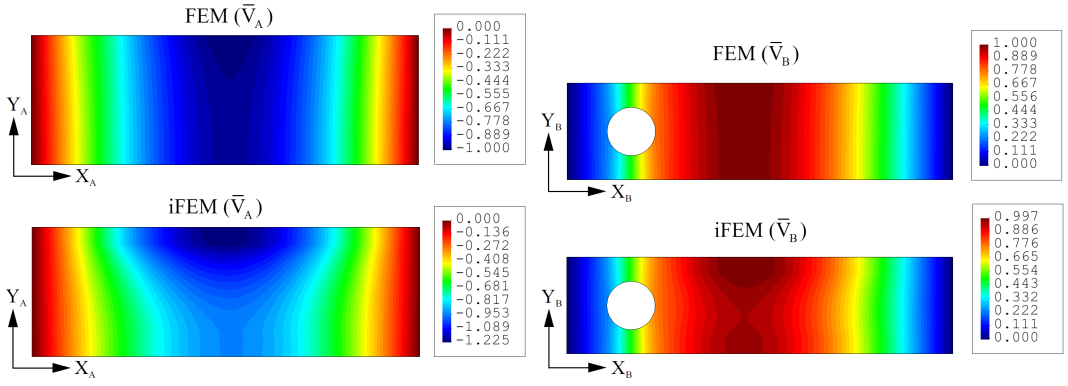

Panel A Panel B

Figure 34. Contour plots of $\bar{V}_A$ and $\bar{V}_B$ displacements for panels A and B: Comparison of high-fidelity FEM and iFEM (Case IV) results.

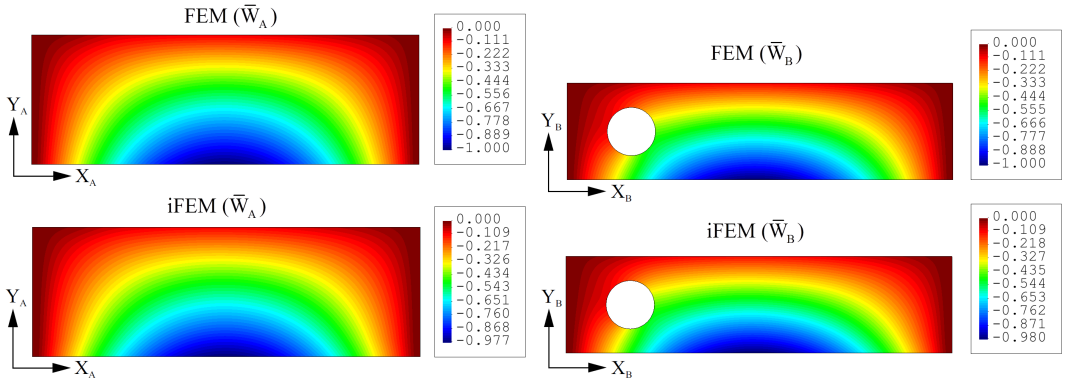

Panel A Panel B

Figure 35. Contour plots of $\bar{W}_A$ and $\bar{W}_B$ displacements for panels A and B: Comparison of high-fidelity FEM and iFEM (Case IV) results.

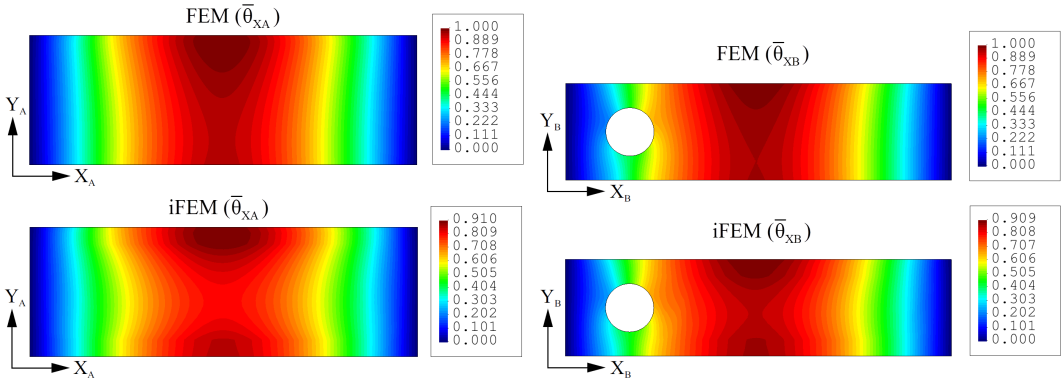

Panel A Panel B

Figure 36. Contour plots of $\bar{\theta}_{XA}$ and $\bar{\theta}_{XB}$ bending rotations for panels A and B: Comparison of high-fidelity FEM and iFEM (Case IV) results.

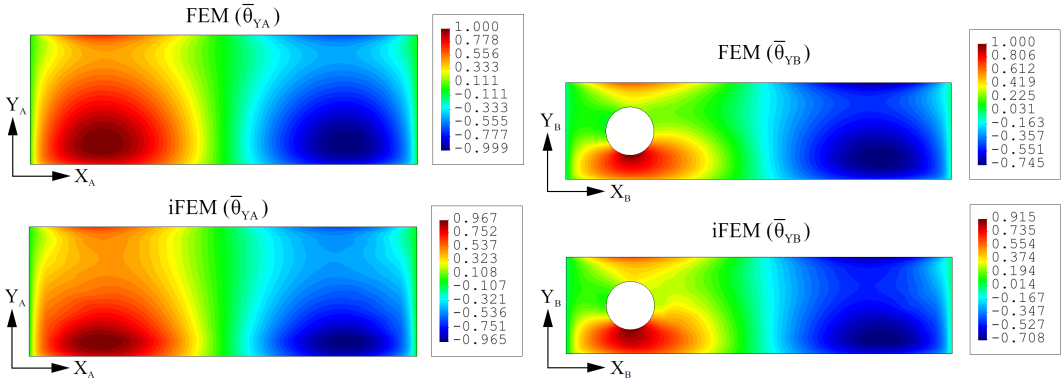

Panel A Panel B

Figure 37. Contour plots of $\bar{\theta}_{YA}$ and $\bar{\theta}_{YB}$ bending rotations for panels A and B: Comparison of high-fidelity FEM and iFEM (Case IV) results.

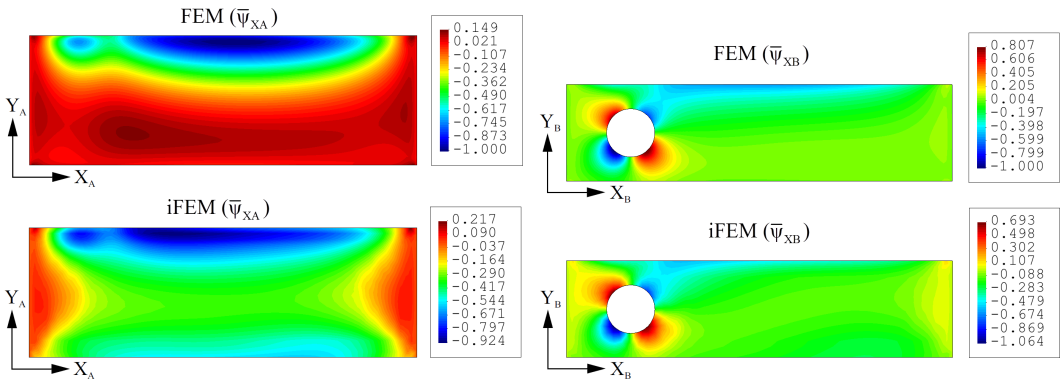

Panel A Panel B

Figure 38. Contour plots of $\bar{\psi}_{XA}$ and $\bar{\psi}_{XB}$ zigzag rotations for panels A and B: Comparison of high-fidelity FEM and iFEM (Case IV) results.

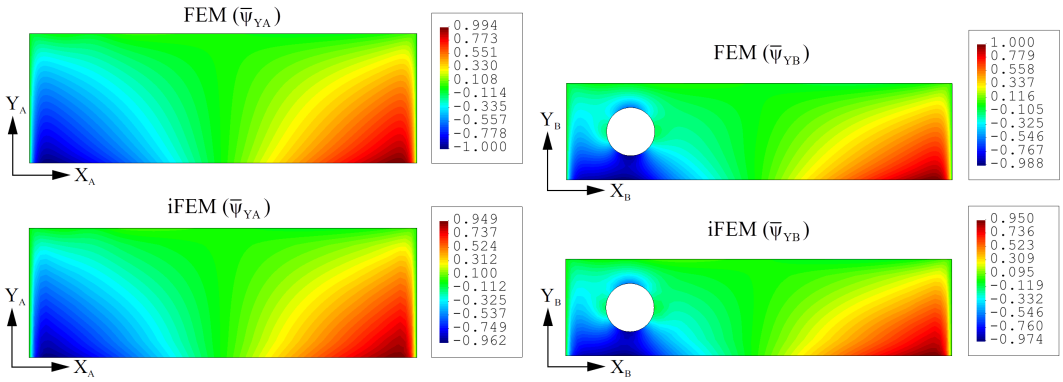

Panel A Panel B

Figure 39. Contour plots of $\bar{\psi}_{YA}$ and $\bar{\psi}_{YB}$ zigzag rotations for panels A and B: Comparison of high-fidelity FEM and iFEM (Case IV) results.

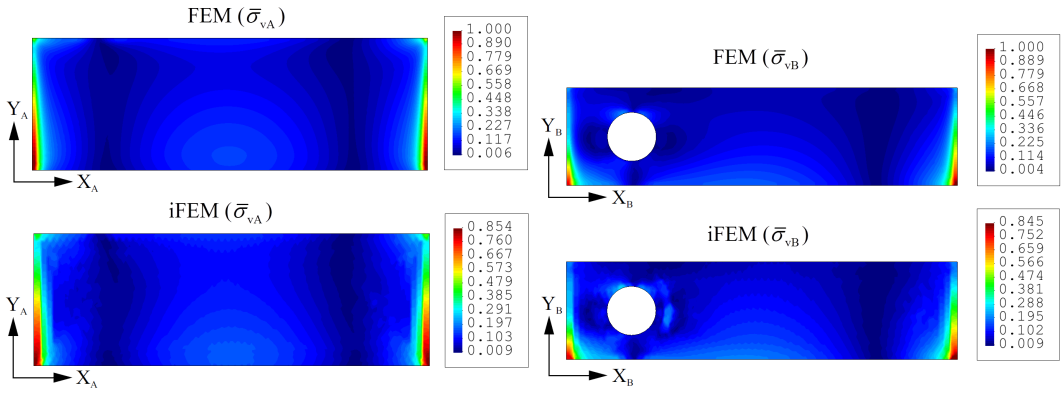

Panel A Panel B

Figure 40. Contour plots of von Mises stresses $\bar{\sigma}_{vA}(Z_A/h=-1)$ and $\bar{\sigma}_{vB}(Z_B/h=1)$ for panels A and B: Comparison of high-fidelity FEM and iFEM (Case IV) results.

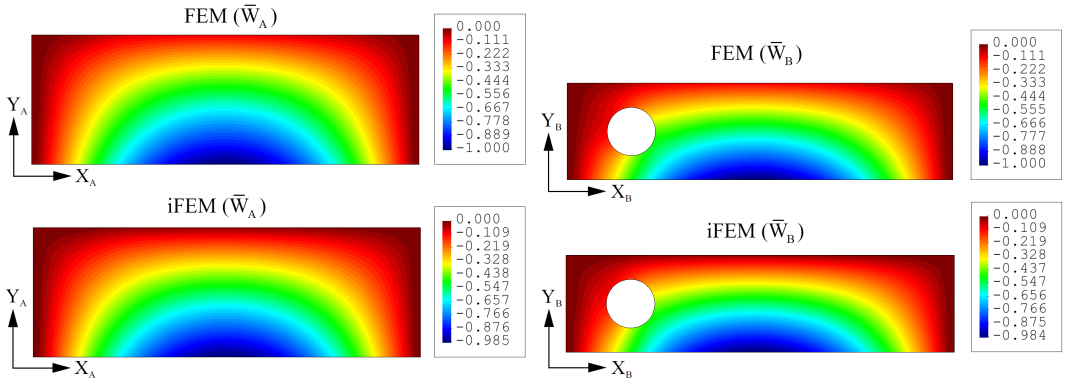

Panel A Panel B

Figure 41. Contour plots of $\bar{W}_A$ and $\bar{W}_B$ displacements for panels A and B: Comparison of high-fidelity FEM and iFEM (Case II-FBG) results.

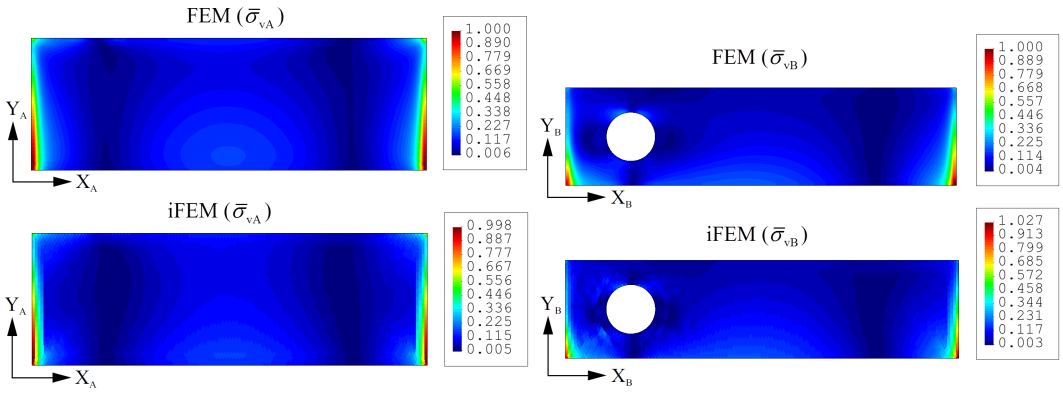

Panel A Panel B

Figure 42. Contour plots of von Mises stresses $\bar{\sigma}_{vA}(Z_A/h=-1)$ and $\bar{\sigma}_{vB}(Z_B/h=1)$ for panels A and B: Comparison of high-fidelity FEM and iFEM (Case II-FBG) results.

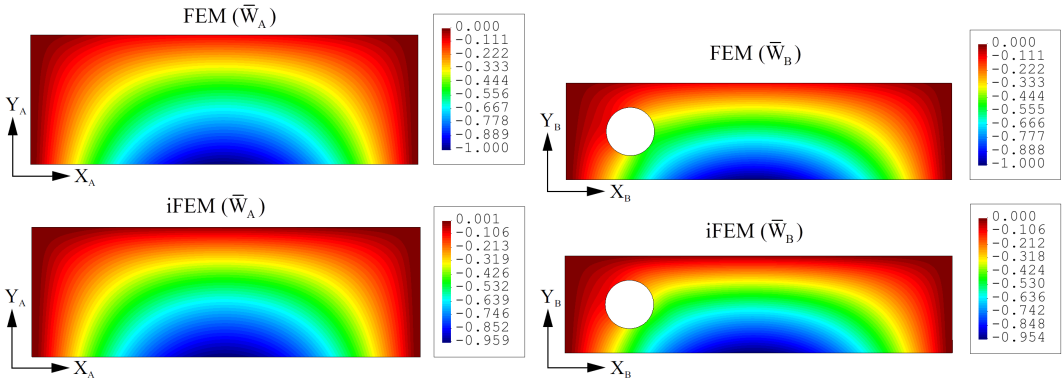

Panel A Panel B

Figure 43. Contour plots of $\bar{W}_A$ and $\bar{W}_B$ displacements for panels A and B: Comparison of high-fidelity FEM and iFEM (Case IV-FBG) results.

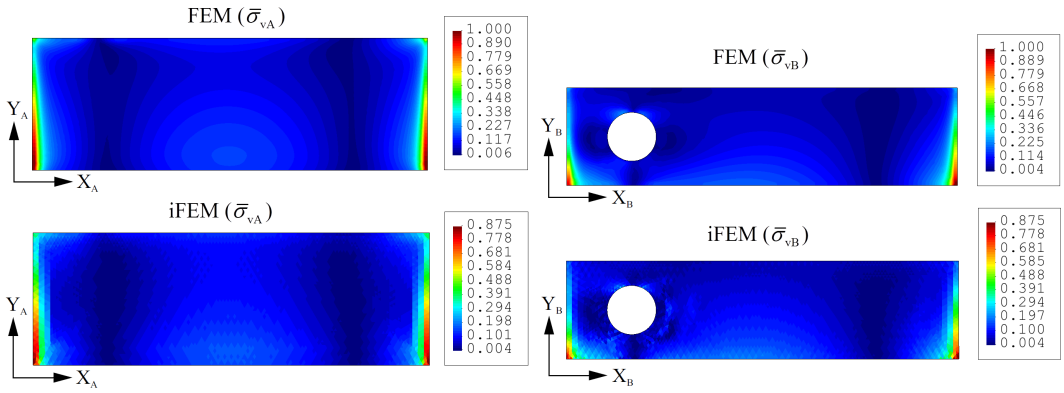

Panel A Panel B

Figure 44. Contour plots of von Mises stresses $\bar{\sigma}_{vA}(Z_A/h=-1)$ and $\bar{\sigma}_{vB}(Z_B/h=1)$ for panels A and B: Comparison of high-fidelity FEM and iFEM (Case IV-FBG) results.

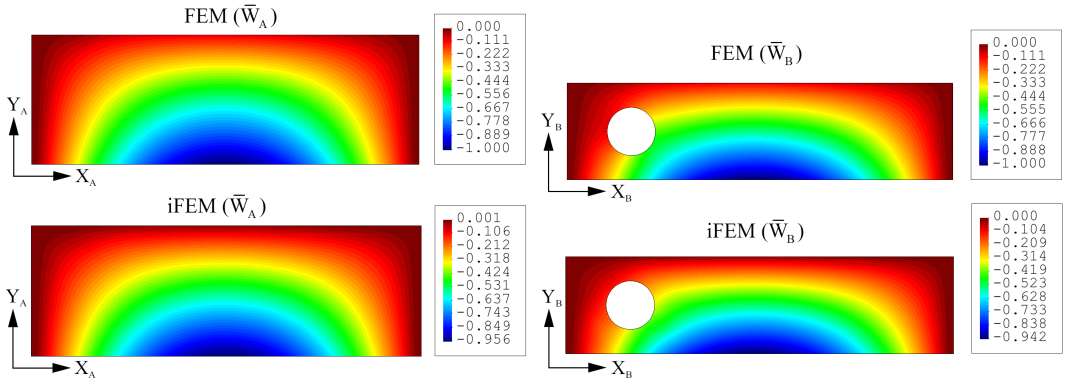

Panel A Panel B

Figure 45. Contour plots of $\bar{W}_A$ and $\bar{W}_B$ displacements for panels A and B: Comparison of high-fidelity FEM and iFEM (Case V-FBG) results.

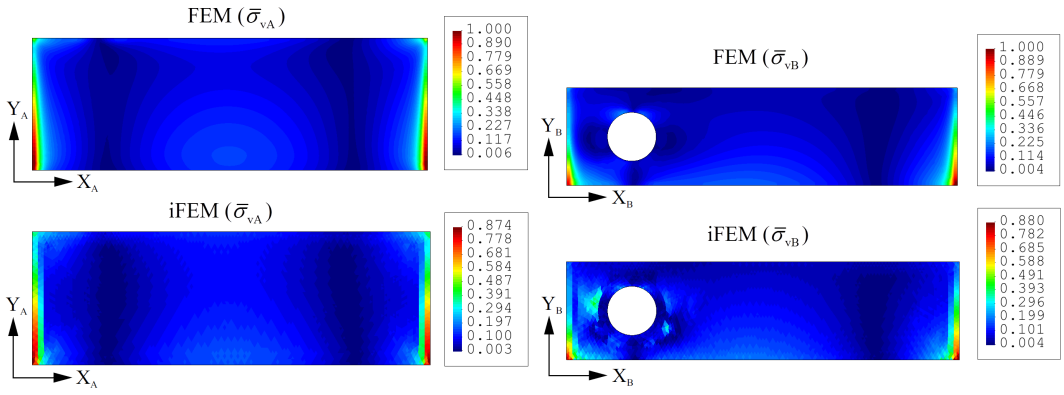

Panel A Panel B

Figure 46. Contour plots of von Mises stresses $\bar{\sigma}_{vA}$ and $\bar{\sigma}_{vB}$ at thickness coordinates $Z_A / h = -1$ and $Z_B / h = 1$ for panels A and B: Comparison of high-fidelity FEM and iFEM (Case V-FBG) results.

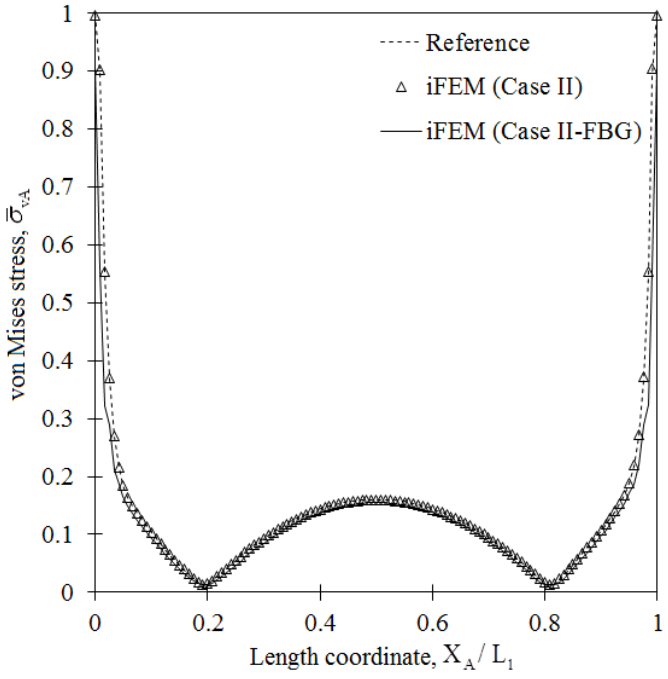

Figure 47. Distribution of von Mises stress $\bar{\sigma}_{vA}$ along length L_1 of panel A: Comparison of high-fidelity FEM and iFEM (Case II) results.

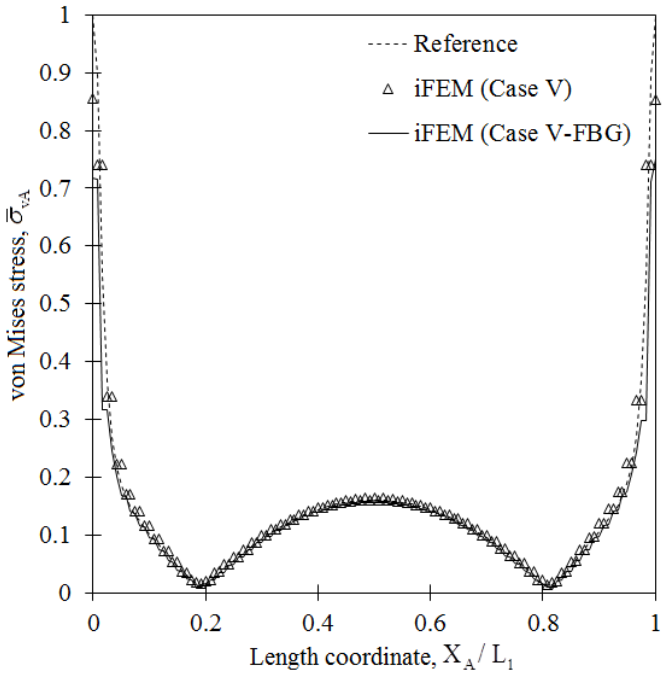

Figure 48. Distribution of von Mises stress $\bar{\sigma}_{vA}$ along length L_1 of panel A: Comparison of high-fidelity FEM and iFEM (Case V) results.

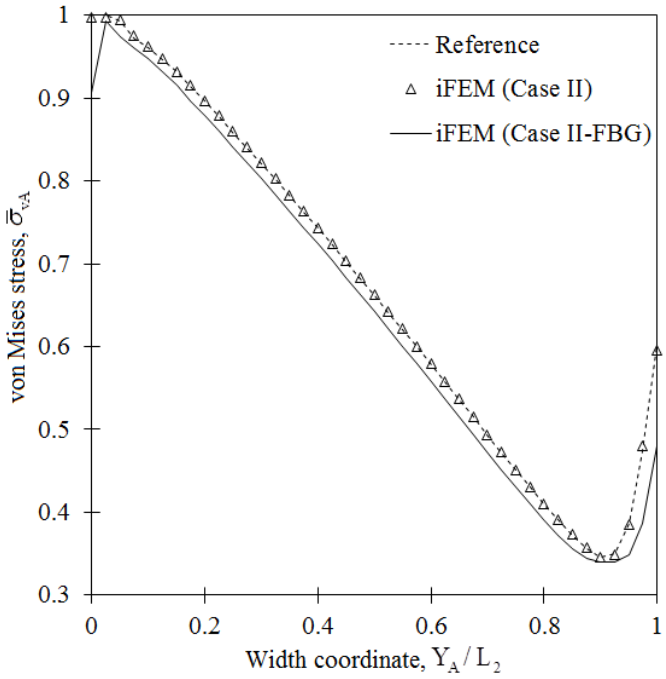

Figure 49. Distribution of von Mises stress $\bar{\sigma}_{vA}$ along width L_2 of panel A: Comparison of high-fidelity FEM and iFEM (Case II) results.

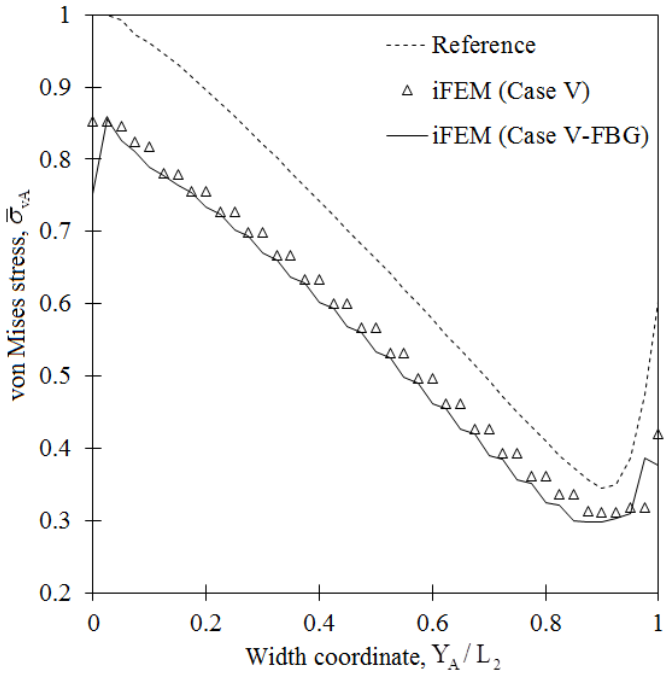

Figure 50. Distribution of von Mises stress $\bar{\sigma}_{vA}$ along width L_2 of panel A: Comparison of high-fidelity FEM and iFEM (Case V) results.